Deep exclusive charged π electroproduction above the resonance region

Murat M. Kaskulov* and Ulrich Mosel
Institut für Theoretische Physik, Universität Giessen, D-35392 Giessen, Germany
(Dated: January 12, 2010)

A description of exclusive charged pion electroproduction $(e, e'\pi^{\pm})$ off nucleons at high energies is proposed. The model combines a Regge pole approach with residual effect of nucleon resonances. The exchanges of $\pi(140)$, vector $\rho(770)$ and axial-vector $a_1(1260)$ and $b_1(1235)$ Regge trajectories are considered. The contribution of nucleon resonances is described using a dual connection between the exclusive hadronic form factors and inclusive deep inelastic structure functions. The model describes the measured longitudinal, transverse and interference cross sections at JLAB and DESY. The scaling behavior of the cross sections is in agreement with JLAB and deeply virtual HERMES data. The results for a polarized beam-spin azimuthal asymmetry in $(\vec{e}, e'\pi^{\pm})$ are presented. Model predictions for JLAB at 12 GeV are given.

PACS numbers: 12.39.Fe, 13.40.Gp, 13.60.Le, 14.20.Dh

arXiv:1001.1952v1 [hep-ph] 12 Jan 2010

I. INTRODUCTION

At JLAB the exclusive reaction $p(e, e'\pi^+)n$ has been studied for a wide range of photon virtualities Q^2 at an invariant mass of the $\pi^+ n$ system around the onset of deep inelastic scattering (DIS) regime, $W \simeq 2$ GeV [1–5]. A separation of the cross section into the transverse $\sigma_{\rm T}$, longitudinal $\sigma_{\rm L}$ and interference $\sigma_{\rm TT}$ and $\sigma_{\rm LT}$ components has been performed. The CLAS data for the polarized beam single-spin asymmetry in $p(\vec{e}, e'\pi^+)n$ are also available [6]. The HERMES data at DESY [7] extend the kinematic region to much higher values of $W^2 > 10$ GeV^2 toward the true DIS region $Q^2 \gg 1$ GeV^2 and much higher values of $-t$. The cross section for $p(e, e'\pi^+)n$ has also been measured above the resonance region at the Cambridge Electron Accelerator (CEA) [8], in $p(e, e'\pi^+)n$ and $n(e, e'\pi^-)p$ at the Wilson Synchrotron Laboratory at Cornell [9–11] and DESY [12–16].

The longitudinal cross section $\sigma_{\rm L}$ is generally thought to be well understood in terms of the pion quasi-elastic knockout mechanism [17] because of the pion pole at low $-t$. If true, this makes it possible to study the charge form factor of the pion at momentum transfer much bigger than in the scattering of pions from atomic electrons [18]. On the other hand, the transverse cross section $\sigma_{\rm T}$ is predicted to be suppressed by $\sim 1/Q^2$ with respect to $\sigma_{\rm L}$ for sufficiently high values of Q^2 and W [19]. On the experimental side, however, the JLAB data show that at forward angles $\sigma_{\rm T}$ is large. For instance, at $Q^2 = 3.91$ GeV^2 [3] $\sigma_{\rm T}$ is by about a factor of two larger than $\sigma_{\rm L}$ and at $Q^2 = 2.15$ GeV^2 it has same size as $\sigma_{\rm L}$ in agreement with previous JLAB measurements [1].

There is a long standing issue concerning the reaction mechanisms contributing to deeply virtual π electroproduction above the resonance region [20–22]. The models which describe $(e, e'\pi^{\pm})$ in terms of hadronic degrees of freedom fail to reproduce $\sigma_{\rm T}$ observed in these reactions, see Ref. [4] and references therein. Previous measurements [1, 2, 11] at smaller and much higher values of Q^2 show a similar problem in the understanding of $\sigma_{\rm T}$. Already from values of $Q^2 > 0.6$ GeV^2 the meson-exchange and/or Regge pole models are not compatible with the measured interference $\sigma_{\rm TT}$ and $\sigma_{\rm LT}$ cross sections and the extraction of the pion form factor relies on the fit to the longitudinal cross section $\sigma_{\rm L}$ only [5]. A remarkably rich experimental data base obtained for $N(e, e'\pi)N'$ above the resonance region remains unexplained [3, 4]. On the other hand, a detailed knowledge of the $p(e, e'\pi^+)n$ reaction above the resonances $\sqrt{s} > 2$ GeV is mandatory for the interpretation of the color transparency signal observed in this reaction off nuclei [23, 24].

A possible description of $\sigma_{\rm T}$ at JLAB has been proposed in Ref. [25]. The approach followed there is to complement the hadron-like interaction types in the t-channel, which dominate in photoproduction and low Q^2 electroproduction, with the direct interaction of virtual photons with partons followed by string (quark) fragmentation into $\pi^+ n$. Then $\sigma_{\rm T}$ can be readily explained and both $\sigma_{\rm L}$ and $\sigma_{\rm T}$ can be described from low up to high values of Q^2. In [25] the reaction $p(e, e'\pi^+)n$ is treated as an exclusive limit, $z \to 1$, of semi-inclusive DIS

$$p(e, e'\pi^+)X \xrightarrow{z\to 1} p(e, e'\pi^+)n \qquad (1)$$

in the spirit of an exclusive-inclusive connection [26]. The transverse cross section in $n(e, e', \pi^-)p$ has been predicted to be smaller than in $p(e, e', \pi^+)n$. The model [27] has also been applied to values of (Q^2, W) in the DIS region at HERMES [7]. In [27] $\sigma_{\rm T}$ in DIS gets much smaller in the forward π^+ production, but still dominates the off-forward region.

However, in [25, 27] the transverse cross section $\sigma_{\rm T}$ itself was modeled and the solution of the problem on the amplitude level is still missing. Both the soft hadronic and hard partonic parts of the amplitude can in principle interfere making non-additive contributions to $\sigma_{\rm L}$ and to interference $\sigma_{\rm TT}$ and $\sigma_{\rm LT}$ cross sections. One might describe this transverse strength in the language of perturbative QCD by considering higher twist correc-

*Electronic address: kaskulov@theo.physik.uni-giessen.de

tions to a generalized parton distribution (GPD) based handbag diagram. This approach has been followed in Ref. [28] where $p(\gamma^*, \pi^+)n$ is considered using the handbag approach with a π-pole contribution. Indeed, the data from JLAB demonstrate [3, 4] that the magnitude and sign of the interference cross sections are not compatible with the simple exchange of a pion trajectory in the t-channel. Because, the contributions from exchange of heavy mesons are small [25] this would suggest the presence of a large transverse resonance or partonic interfering background to the meson-pole contributions.

In this work we attempt a phenomenological approach to model the hard scattering or, using a duality argument, the presence of nucleon resonances beyond the t-channel meson-pole amplitudes. The meson-exchange processes dominate in high-energy photoproduction and low Q^2 electroproduction above the resonance region. One way to describe this region is to assume that the coherent sum of baryon resonance contributions would be expected by duality arguments to be equivalent to a sum over t-channel Regge trajectories. However, in electroproduction, with plausible assumptions concerning the coupling constants and transition form factors, the exchange of heavy mesons alone does not explain the transverse cross section and turns out to be marginal [25]. It is also a generic rule that single t-channel meson-exchange processes vanish in the forward π^+ direction. On the other hand, pion exchange does play an important role at near forward directions and must be included, as must be the nucleon-pole charge term to satisfy gauge invariance. The nucleon magnetic transitions vanish in the forward production and can be neglected [29]. For instance, in photoproduction this suggests an extreme phenomenological scenario, known as an electric model, where the only relevant contributions to $\pi^\pm$ production at forward angles are the ones from π-exchange and the nucleon Born term where the inclusion of the latter is mandatory to conserve gauge invariance.

By reggeization of the π-exchange one takes into account higher mass and higher spin excitations. At forward angles considered here the momentum transfer $-t$ is small and the exchanged π-trajectory is close to its first materialization. However, the nucleons in the $s(u)$-channel pole amplitudes are highly off-mass-shell and with increasing values of (Q^2, W) the effect of nucleon resonances should become more and more important. This is because of the well known hardening of the higher mass resonance transition form factors which must respect the scaling properties of deep inelastic structure functions in inclusive scattering [30, 31]. We shall follow this suggestion and model the contribution of nucleon resonances using a local Bloom-Gilman connection between the exclusive and inclusive processes.

Another question which we address here is a possible contribution of the resonance (or partonic) background to the longitudinal cross section $\sigma_{\rm L}$ which is presently used to get the information about the pion form factor. Indeed, the same *resonance/partonic* background also affects the longitudinal cross section making the π-pole dominance in the longitudinal response rather questionable. Based on a quantitative description of electroproduction data achieved in this work in a large range of (Q^2, W) from JLAB to DIS region at HERMES the present results may assist in the experimental analysis and extraction of the pion charge form factor to minimize systematic uncertainties. Recall that it is essential to use theoretical model input for the extraction of the pion form factor [5].

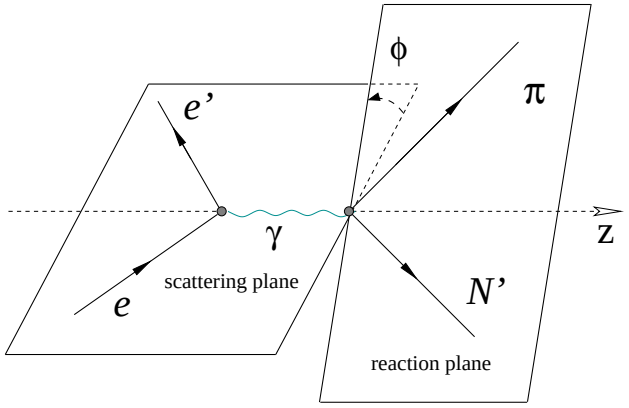

FIG. 1: Exclusive reaction $N(e, e'\pi)N'$ in the laboratory. ϕ stands for the azimuthal angle between the electron scattering (e, e') plane and reaction $N(\gamma^*, \pi)N'$ plane.

The outline of the present paper is as follows. In the Section II we briefly recall the kinematics and definition of the cross sections in exclusive $(e, e'\pi^\pm)$ electroproduction reaction. In Section III we discuss our treatment of gauge invariant π-exchange in the Regge pole model. In Section IV we consider the effect of nucleon resonances and derive the transition form factors using an exclusive-inclusive connection. In Section V we consider the contribution of vector $\rho(770)$ and axial-vector $a_1(1260)$ and $b_1(1235)$ Regge trajectories. In Section VI we briefly discuss the $\pi^\pm$ photoproduction at forward angles. Then the model is extended to electroproduction. In Sections VII-IX the results are compared to the experimental data from JLAB, DESY and Cornell. In Section X we compare our results with the HERMES data. The Q^2 behavior of the cross sections is studied in Section XI. The polarized beam-spin asymmetry and the role played by the axial-vector mesons in $(\vec{e}, e'\pi^\pm)$ are discussed in Section XII. In Section XIII the model predictions for JLAB at 12 GeV are presented. The conclusions are summarized in Section XIV. Some details of the calculations are relegated to the Appendix.

II. KINEMATICS AND DEFINITIONS

We recall briefly the kinematics in exclusive π electroproduction

$$e(l) + N(p) \to e'(l') + \pi(k') + N'(p'), \qquad (2)$$

and specify the notations and definitions of variables. The reaction (2) in the laboratory is shown in Figure 1 where the target nucleon is at rest, the z-axis is directed along the three momentum $\vec{q} = (0, 0, \sqrt{\nu^2 + Q^2})$ of the exchanged virtual photon γ^* with $q = l - l' = (\nu, \vec{q})$, $Q^2 = -q^2$, $\nu = E_e - E'_e$ and $l(l')$ is the four momentum of incoming (deflected) electrons. In Figure 1 ϕ stands for the azimuthal angle between the electron scattering (e, e') plane and $\gamma^* N \to \pi N'$ reaction plane. ϕ is zero when the pion is closest to the outgoing electron [32].

In exclusive reaction $(e, e'\pi)$ we shall deal with an unpolarized target and, both unpolarized and polarized lepton beams. The differential cross section is given by

$$\begin{aligned}\frac{d\sigma}{dQ^2 d\nu dt d\phi} &= \frac{\Phi}{2\pi}\left[\frac{d\sigma_{\rm T}}{dt} + \varepsilon\frac{d\sigma_{\rm L}}{dt}\right.\\ &+ \sqrt{2\varepsilon(1+\varepsilon)}\frac{d\sigma_{\rm LT}}{dt}\cos(\phi)\\ &+ \varepsilon\frac{d\sigma_{\rm TT}}{dt}\cos(2\phi)\\ &+ \left. h\sqrt{2\varepsilon(1-\varepsilon)}\frac{d\sigma_{\rm LT'}}{dt}\sin(\phi)\right], \qquad (3)\end{aligned}$$

where $d\sigma_{\rm T}$ is the transverse cross section, $d\sigma_{\rm L}$ is the longitudinal cross section, $d\sigma_{\rm TT}$ is the cross section originating from the interference between the transverse components of the virtual photon, $d\sigma_{\rm LT}$ is the cross section arising from the interference between the transverse and longitudinal polarizations of the virtual photon and $d\sigma_{\rm LT'}$ is the beam-spin polarized cross section resulting from the interference between the transverse and longitudinal photons and helicity $h = \pm 1$ of the incoming electron.

The virtual photon flux is conventionally defined as [33]

$$\Phi = \frac{\pi}{E_e(E_e - \nu)}\left(\frac{\alpha_e}{2\pi^2}\frac{E_e - \nu}{E_e}\frac{\mathcal{K}}{Q^2}\frac{1}{1-\varepsilon}\right), \qquad (4)$$

with $\alpha_e \simeq 1/137$, $\mathcal{K} = (W^2 - M_N^2)/2M_N$ and

$$\varepsilon = \frac{1}{1 + 2\frac{\nu^2+Q^2}{4E_e(E_e-\nu)-Q^2}} \qquad (5)$$

is the ratio of longitudinal to transverse polarization of the virtual photon. The longitudinal/transverse (L/T) separated virtual-photon nucleon cross sections are given in Appendix A. The t-differential cross section for $N(\gamma^*, \pi)N'$ integrated over ϕ is denoted here as

$$\frac{d\sigma_{\rm U}}{dt} = \frac{d\sigma_{\rm T}}{dt} + \varepsilon\frac{d\sigma_{\rm L}}{dt}. \qquad (6)$$

The longitudinal beam single-spin asymmetry (SSA) in $(\vec{e}, e'\pi)$ scattering is defined so that

$$A_{\rm LU}(\phi) \equiv \frac{d\sigma^{\rightarrow}(\phi) - d\sigma^{\leftarrow}(\phi)}{d\sigma^{\rightarrow}(\phi) + d\sigma^{\leftarrow}(\phi)}, \qquad (7)$$

where $d\sigma^{\rightarrow}$ refers to positive helicity $h = +1$ of the incoming electron. The azimuthal moment associated with the beam SSA is given by [32]

$$A_{\rm LU}^{\sin(\phi)} = \frac{\sqrt{2\varepsilon(1-\varepsilon)}d\sigma_{\rm LT'}}{d\sigma_{\rm T} + \varepsilon d\sigma_{\rm L}}. \qquad (8)$$

III. GAUGING THE PION EXCHANGE

The diagrams describing the π^+ and/or π^- electroproduction amplitudes in exclusive reactions $p(e, e'\pi^+)n$ and $n(e, e'\pi^-)p$ are shown in Figure 2. At high energies the particles exchanged in the t-channel are understood as the Regge trajectories. In $p(e, e'\pi^+)n$ the s-channel nucleon-pole term (IB diagram) is added to the t-channel π-pole exchange (IA diagram) to conserve the charge of the system. Similarly, the diagram IIA and the u-channel nucleon-pole diagram IIB form a gauge invariant amplitude in $n(e, e'\pi^-)p$. The last two diagrams (III and IV) correspond to the exchange of vector $V = \rho(770)$ and axial-vector $A = a_1(1260)$, $b_1(1235)$ Regge trajectories.

The π-exchange currents describing the reactions $p(\gamma^*, \pi^+)n$ and $n(\gamma^*, \pi^-)p$ take the form [24]

$$\begin{aligned}-iJ_s^{\mu}(\gamma^* p \to \pi^+ n) = \sqrt{2}g_{\pi NN}\,\bar{u}_{s'}(p')\gamma_5\left[\mathcal{F}_{\gamma\pi\pi}(Q^2,t)\frac{(k+k')^{\mu}}{t - m_{\pi}^2 + i0^+} + \mathcal{F}_s(Q^2,s,t)\frac{(p+q)_{\sigma}\gamma^{\sigma}\gamma^{\mu} + M_p\gamma^{\mu}}{s - M_p^2 + i0^+}\right.\\ \left. + [\mathcal{F}_{\gamma\pi\pi}(Q^2,t) - \mathcal{F}_s(Q^2,s,t)]\frac{(k-k')^{\mu}}{Q^2}\right]u_s(p), \qquad (9)\end{aligned}$$

$$\begin{aligned}-iJ_u^{\mu}(\gamma^* n \to \pi^- p) = -\sqrt{2}g_{\pi NN}\,\bar{u}_{s'}(p')\left[\mathcal{F}_{\gamma\pi\pi}(Q^2,t)\frac{(k+k')^{\mu}}{t - m_{\pi}^2 + i0^+} - \mathcal{F}_u(Q^2,u,t)\frac{\gamma^{\mu}(p'-q)_{\sigma}\gamma^{\sigma} + M_p\gamma^{\mu}}{u - M_p^2 + i0^+}\right.\\ \left. + [\mathcal{F}_{\gamma\pi\pi}(Q^2,t) - \mathcal{F}_u(Q^2,u,t)]\frac{(k-k')^{\mu}}{Q^2}\right]\gamma_5 u_s(p), \qquad (10)\end{aligned}$$

where $\mathcal{F}_{\gamma\pi\pi}(Q^2,t)$ denotes the transition form factor of the pion and $\mathcal{F}_{s(u)}(Q^2, s(u), t)$ stands for the proton $s(u)$-channel transition form factor. In Eqs. (9) and (10) $g_{\pi NN} = 13.4$ is the pseudoscalar πN coupling constant, $t = k^2$, $s = W^2$, $k = k' - q = p - p'$ and other notations are obvious.

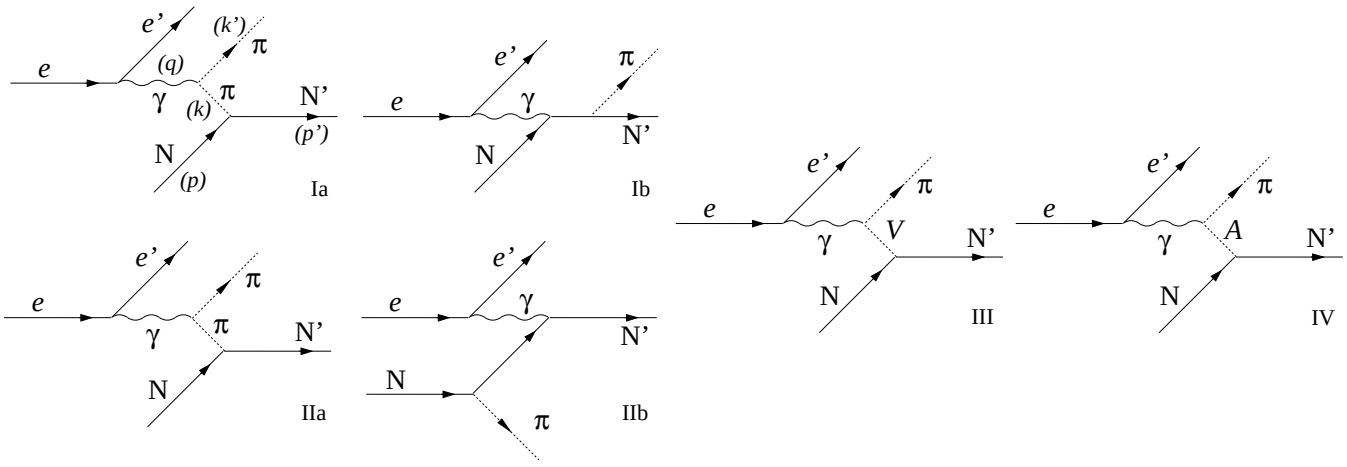

FIG. 2: The diagrams describing the π^+ and/or π^- electroproduction amplitudes in exclusive reactions $p(e,e'\pi^+)n$ and $n(e,e'\pi^-)p$. In $p(e,e'\pi^+)n$ the s-channel nucleon-pole term (IB diagram) is added to the t-channel π-pole exchange (IA diagram) to conserve the charge of the system. Similarly, the diagram IIA and the u-channel nucleon-pole diagram IIB form gauge invariant amplitude in $n(e,e'\pi^-)p$. The last two diagrams (III and IV) correspond to the exchange of vector $V=\rho(770)$ and axial-vector $A=a_1(1260)$ and $b_1(1235)$ Regge trajectories. The momentum flows are shown in the diagram IA.

The amplitudes are gauge invariant and the current conservation condition, $q_\mu J^\mu_{s(u)}=0$, is satisfied in the presence of different form factors, $\mathcal{F}_{\gamma\pi\pi}$ and $\mathcal{F}_{s(u)}$, which in general can depend on values of $(Q^2,s(u),t)$. Eqs. (9) and (10) are obtained using the requirement that the modified electromagnetic vertex functions entering the amplitude obey the same Ward-Takahashi identities as the bare ones [34–36]. Further aspects concerning the gauged electric amplitude are relegated to Appendix B.

At high energies the exchange of high-spin and high-mass particles lying on the π-Regge trajectory has to be taken into account. Then, to continue the electric amplitude to high energies we define the half off-shell form factor

$$\mathcal{F}_{\gamma\pi\pi}(Q^2,t)=F_{\gamma\pi\pi}(Q^2)(t-m_\pi^2)\mathcal{R}(\alpha_\pi(t)). \tag{11}$$

In the π-pole term this procedure replaces the Feynman propagator by the Regge propagator suggested by the high energy limit of the amplitude

$$\mathcal{D}(t)=\frac{1}{t-m_\pi^2+i0^+}\Longrightarrow\mathcal{R}(\alpha_\pi(t))=\left[\frac{1+e^{-i\pi\alpha_\pi(t)}}{2}\right](-\alpha'_\pi)\,\Gamma[-\alpha_\pi(t)]e^{\alpha_\pi(t)\ln(\alpha'_\pi s)}, \tag{12}$$

where $\alpha_\pi(t)=\alpha'_\pi(t-m_\pi^2)$ is the Regge trajectory of π with a slope $\alpha'_\pi=0.74$ GeV^{-2} and Γ function results from suppression of singularities in the physical region. Close to the pole position $t\to m_\pi^2$ the Regge propagator is reduced to $1/(t-m_\pi^2)$ and we approach the Feynman amplitude describing the first $\pi(140)$ materialization of the trajectory.

We further treat the nucleon-pole part as an indispensable part of the π-pole amplitude. At the real photon point gauge invariance requires for the nucleon-pole term the same phase and t-dependence as in the π-Regge amplitude [29]

$$\mathcal{F}_{s(u)}(Q^2,s(u),t)=F_{s(u)}(Q^2,s(u))(t-m_\pi^2)\mathcal{R}(\alpha_\pi(t)). \tag{13}$$

This assumption is justified by the observation that there exists a gauge where the π-exchange vanishes and the π-pole contribution is generated kinematically by the nucleon-pole term itself [37].

For the pion transition form factor $F_{\gamma\pi\pi}$ we use a monopole parameterization

$$F_{\gamma\pi\pi}(Q^2)=[1+Q^2/\Lambda^2_{\gamma\pi\pi}]^{-1}, \tag{14}$$

with a cut-off $\Lambda_{\gamma\pi\pi}$ as a fit parameter. In general, the cut-off can be a function of t, $\Lambda_{\gamma\pi\pi}=\Lambda_{\gamma\pi\pi}(t)$, reflecting the off-shellness of the pion in the t-channel and the underlying space-time pattern of direct partonic interactions at high values of $-t$ [38]. In the forward π^+ production the momentum transfer t is rather small and the exchanged pion is close to its mass shell. In the fit to data we shall not allow large deviations from the VMD value.

Since the π-pole contribution is replaced by an exchange of reggeon-pion, the relation to the on-shell pion form factor might be lost [39] and $F_{\gamma\pi\pi}(Q^2)$ should be understood as an effective transition form factor.

IV. EFFECT OF NUCLEON RESONANCES

Similar arguments should apply to the transition form factor in the $s(u)$-channel nucleon-pole terms. A simplest choice would be to use in Eq. (13)

$$F_{s(u)}(Q^2, s(u)) = F_1^p(Q^2), \tag{15}$$

where $F_1^p(Q^2)$ is the proton Dirac form factor. However, since the nucleon is highly of-mass-shell this assumption might be too naive [40]. Indeed, this prescription underestimates the JLAB data for $\sigma_{\rm T}$ [25] and results in a wrong interference pattern between L/T components.

A way to model an intermediate state which is highly off-mass-shell is to increase the Fock space available for the virtual nucleon allowing the latter to excite into resonances. Similar to the reggeized-exchange, these resonances with higher masses and spins may lie on the nucleon Regge trajectory or correspond to higher mass states with the same angular momentum as the nucleon. We replace the Born term in the s-channel for π^+ production by a sum over all resonance excitations

$$\frac{F_s(Q^2, M_p)}{s - M_p^2 + i0^+} \to \sum_i r(M_i)c(M_i)\frac{F(Q^2, M_i^2)}{s - M_i^2 + i0^+}, \tag{16}$$

where the sum runs from the nucleon-pole contribution, M_i is the ith resonance mass, r and c are the electromagnetic and strong couplings, respectively, relative to the lowest lying nucleon state, *e.g.* $r(M_p)c(M_p) = 1$. For π^- production we use a similar expansion over the u-channel contributions

$$\frac{F_u(Q^2, M_p)}{u - M_p^2 + i0^+} \to \sum_i r(M_i)c(M_i)\frac{F(Q^2, M_i^2)}{u - M_i^2 + i0^+}. \tag{17}$$

In the region of interest for the experiments to be discussed later in this paper the invariant mass is $W \gtrsim 2$ GeV and thus in a region where the DIS regime starts. In order to make a connection to our earlier work in which we modeled the transverse cross section by a partonic subprocess [25, 27] we now invoke duality for the exclusive processes treated here. We start with the Bloom-Gilman duality [31] in the local form

$$F_2^p(x_{\rm B}, Q^2) = \sum_i (M_i^2 - M_p^2 + Q^2)W(Q^2, M_i)\delta(s - M_i^2), \tag{18}$$

where $x_{\rm B}$ stands for a Bjorken scaling variable and the deep inelastic structure function $F_2^p(x_{\rm B}, Q^2)$ is expressed as a sum of resonances. In Eq. (18) the hadronic basis is used as a substitute for the quark basis. When Q^2 is large the bulk structure of the resonances becomes less and less important and we are justified when taking the zero-width approximation [41]. $W(Q^2, M_i)$ defines the ith resonance contribution to the $\gamma^* p$ forward scattering amplitude; it is essentially the electromagnetic coupling constant $r(M_i)$ times a resonance form factor $F(Q^2, M_i)$ normalized to unity at $Q^2 = 0$ [42]:

$$W(Q^2, M_i) = r^2(M_i)[F(Q^2, M_i)]^2, \quad F(0, M_i) = 1. \tag{19}$$

A resonance with mass M_i contributes to the structure function at Bjorken $x_i = Q^2/(M_i^2 - M_p^2 + Q^2)$.

To be in line with measurements in the DIS region the resonance form factors $F(Q^2, M_i^2)$ must fall with Q^2 at least as fast as the nucleon dipole form factor. Futhermore, to be consistent with the scaling behavior of deep inelastic structure functions the cut-off in the dipole transition form factors must increase as the mass of the resonance is increases [30, 42]. Therefore we assume [41]

$$F(Q^2, M_i^2) = \left(\frac{1}{1 + \xi\frac{Q^2}{M_i^2}}\right)^2, \tag{20}$$

where the value of ξ is a common average cut-off parameter. This scenario suggests a hardening of the resonance form factors with increasing value of M_i [42].

At high energies the level density of resonances $\rho(M_i^2)$ is large and we can replace the sum in Eq. (18) over discrete spectrum of resonances by a continuous integral

$$\sum_i \to \int_{M_p^2}^{\infty} dM_i^2 \rho(M_i^2). \tag{21}$$

This is clearly a rough approximation in the resonance region itself, but it makes no difference when we restrict ourselves to the experimental data above the resonance region. Performing the integration over M_i yields

$$F_2^p(x_{\rm B}, Q^2) = (s - M_p^2 + Q^2)r^2(s)[F(Q^2, s)]^2\rho(s). \tag{22}$$

The structure function F_2^p can be written in the form of a polynomial in $1 - 1/\omega'$ where $\omega' = 1 + W^2/Q^2$ is a Bloom-Gilman variable. As $Q^2/W^2 \to \infty$ or $\omega' \to 1$ the leading term yields the Drell-Yan-West behavior

$$F_2^p(\omega') \propto (\omega' - 1)^3, \tag{23}$$

which shows that the power law behavior of the form factor is related to the suppression of the structure functions in the limit where one quark carries all of the hadron's momentum. The approximation (23) is supposed to be reasonable down to $x_{\rm B} \simeq 0.2$. Expanding the resonance form factors for $\omega' \to 1$ the leading term reads

$$F(Q^2, s) = \frac{(\omega' - 1)^2}{\xi^2} + \mathcal{O}((\omega' - 1)^3). \tag{24}$$

The duality relation, Eq. (22), can be written in the form

$$(\omega' - 1)^3 \propto Q^2\frac{(\omega' - 1)^4}{\xi^4}r^2(s)\rho(s). \tag{25}$$

This translates into

$$r^2(s)\rho(s) \propto \frac{1}{Q^2(\omega' - 1)} = \frac{1}{s}. \tag{26}$$

Since the level density grows with increasing s, for instance, $\rho \propto \exp(const \times M_i)$, the coupling strength to

resonances is decreasing, *i.e*, $r(s_i) \propto (s_i \rho(s_i))^{-1/2}$ where $s_i = M_i^2$. This simple result has a remarkable consequence. Although an infinite tower of resonances can contribute to the structure function the weight of resonances decreases as $1/s$ with increasing value of s.

A vanishing coupling of the higher spin (mass) resonances to πN is expected from the chiral phenomenology [43]. The latter claim is consistent with our observation that the more we excite the nucleon the less it decays into the exclusive channel. Assuming for the strong coupling a similar form $c(s_i) \propto (s_i^{(2\beta-1)} \rho(s_i))^{-1/2}$ with $\beta \geq 1$ the integration in Eqs. (16) and (17) is superconvergent and can be carried out analytically. Without an explicit assumption about the behavior of the level density we get the following form for the product

$$\rho(s_i)\, r(s_i) c(s_i) = \frac{1}{\lambda} s_i^{-\beta}, \tag{27}$$

where λ is a normalization constant and $\beta \geq 1$ accounts for the behaviour of coupling constants as well as a deviation of the level density contributing to the exclusive channel compared to the total inclusive density of states.

We now absorb all the effects of the higher lying resonances into the nucleon-pole term by setting

$$\sum_i r(M_i) c(M_i) \frac{F(Q^2, M_i^2)}{s - M_i^2 + i0^+} \Longrightarrow \int\limits_{M_p^2}^{\infty} dM_i^2 \rho(M_i^2) r(M_i^2) c(M_i^2) \frac{F(Q^2, M_i^2)}{s - M_i^2 + i0^+}$$
$$= \int\limits_{M_p^2}^{\infty} ds_i \frac{s_i^{-\beta}}{\lambda} \frac{F(Q^2, s_i)}{s - s_i + i0^+} \equiv \frac{F_s(Q^2, s)}{s - M_p^2 + i0^+}, \tag{28}$$

where the sum in Eq. (16) over discrete spectrum of resonances has been replaced again by a continuous integral. $F_s(Q^2, s)$ is the form factor on the *r.h.s.* of Eq. (13). Similarly we proceed for the transition form factor $F_u(Q^2, u)$ in the u-channel, Eq. (17). The integration covers the full region from the nucleon pole M_p up to ∞. Furthermore, the normalization constants λ are determined by the charge conservation at the real photon point $Q^2 = 0$, *i.e.*

$$\lambda\Big|_{s-channel} = (s - M_p^2) \int\limits_{M_p^2}^{\infty} ds_i \frac{\rho(s_i)\, r(s_i) c(s_i)}{s - s_i + i0^+}, \tag{29}$$

$$\lambda\Big|_{u-channel} = (u - M_p^2) \int\limits_{M_p^2}^{\infty} ds_i \frac{\rho(s_i)\, r(s_i) c(s_i)}{u - s_i^2 + i0^+}, \tag{30}$$

for the s- and u-channels, respectively. This merely guarantees that the effective form factors are normalized to unity, *e.g.* $F_{s(u)}(0, s(u)) = 1$. With this prescription we demand that the contributions of resonances show up in the modified off-mass-shell behavior of the nucleon transition form factors.

The s- and u-channel form factors read

$$F_s(Q^2, s) = \frac{\int\limits_{M_p^2}^{\infty} ds_i \frac{s_i^{-\beta}}{s - s_i + i0^+} \left(\frac{1}{1 + \xi \frac{Q^2}{s_i}} \right)^2}{\int\limits_{M_p^2}^{\infty} ds_i \frac{s_i^{-\beta}}{s - s_i + i0^+}}, \tag{31}$$

$$F_u(Q^2, u) = \frac{\int\limits_{M_p^2}^{\infty} ds_i \frac{s_i^{-\beta}}{u - s_i + i0^+} \left(\frac{1}{1 + \xi \frac{Q^2}{s_i}} \right)^2}{\int\limits_{M_p^2}^{\infty} ds_i \frac{s_i^{-\beta}}{u - s_i + i0^+}}, \tag{32}$$

Because of the singularity at $s_i = s + i0^+$ the s-channel integrals develop an imaginary part which is missing in the u-channel contribution where the branch point sits in the unphysical region.

Concerning the terminology for regions like the one at JLAB it would be appropriate to use the words *resonance* effect. On the other hand, in the DIS region at HERMES it would be more natural to describe the effect as of *partonic* origin. Since both descriptions are dual in the context of the present approach we shall in line of [25, 27] refer to the terms derived above as the *resonance/partonic* (R/P) contributions.

V. VECTOR AND AXIAL-VECTOR REGGE TRAJECTORIES

The mesonic Regge trajectories can be characterized by the signature and parity. The signature determines whether the Regge poles in the scattering amplitude will

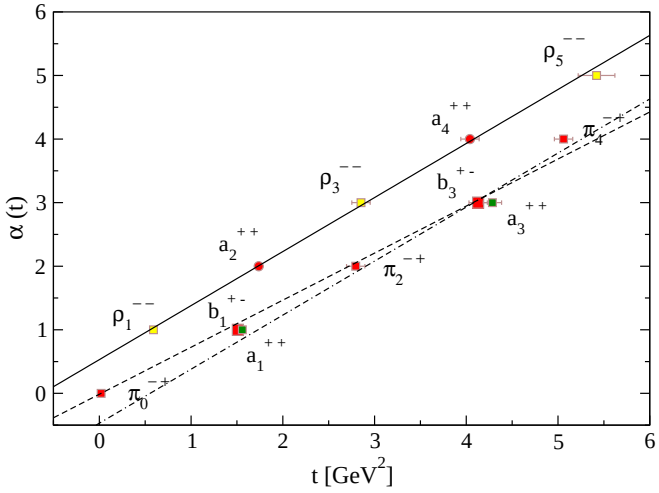

FIG. 3: (Color online) $\rho(770)/a_2(1320)$ (solid), $\pi/b_1(1235)$ (dashed) and $a_1(1260)$ (dash-dotted) Regge trajectories.

occur for even or odd positive integer value of the trajectory $\alpha(t) = J$ (the spin). The leading mesons contributing to $(e, e'\pi^{\pm})$ are the natural $P = (-1)^J$ parity vector $\rho(770)$ and the unnatural $P = (-1)^{J+1}$ parity axial-vector mesons $a_1(1260)$ and $b_1(1235)$. The Regge trajectories $\alpha(t)$ considered here are shown in Figure 3

The absolute contribution of the reggeized ρ-exchange amplitude to $(e, e'\pi^{\pm})$ turns out to be small, but by its interference with the s- and u-channel terms considered above, it is responsible for the π^-/π^+ asymmetry in photoproduction and gives a sizable contribution to the π^-/π^+ ratio in electroproduction.

In the axial-vector sector, the experimental isolation of the amplitudes with axial-vector quantum numbers would be of great interest. For instance, using a proton target polarized perpendicular to the reaction plane, and photons polarized parallel to the reaction plane, one can directly access the difference between recoil and the polarized target asymmetries which is proportional to the exchange of the $a_1(1260)$-trajectory [44]. However, being suppressed by the Regge factor $\sim e^{-\alpha'_{a_1}\ln(\alpha'_{a_1}s)m^2_{a_1}}$ at $t = 0$, its contribution to the forward unpolarized cross section turns out to be small. With our choice of the b_1NN tensor coupling the contribution of $b_1(1235)$ exchange is even smaller. On the other hand, as we shall see, it is absolutely essential to consider the exchange of $a_1(1260)$ Regge trajectory in the polarization $(\vec{e}, e'\pi)$ observables like the beam spin azimuthal asymmetry considered in the following. Other aspects related to a possible role of $a_1(1260)$ in $(e, e'\pi)$ are discussed in [45].

A. Vector-isovector $I^G(J^{PC}) = 1^+(1^{--})$ exchange currents

The currents J^μ_ρ describing the exchange of the natural parity $\rho(770)$-meson Regge trajectory are given by

$$\begin{bmatrix} -iJ^\mu_\rho(\gamma^* p \to \pi^+ n) \\ \\ -iJ^\mu_\rho(\gamma^* n \to \pi^- p) \end{bmatrix} = -i\ \sqrt{2} G_{\rho\gamma\pi}\, G_{\rho NN} F_{\rho\gamma\pi}(Q^2) \varepsilon^{\mu\nu\alpha\beta} q_\nu k_\alpha \bar{u}_{s'}(p') \left[(1+\kappa_\rho)\gamma_\beta - \frac{\kappa_\rho}{2M_p}(p+p')_\beta\right] u_s(p)$$
$$\times \left[\frac{1 - e^{-i\pi\alpha_\rho(t)}}{2}\right] \left(-\alpha'_\rho\right) \Gamma[1-\alpha_\rho(t)] e^{\ln(\alpha'_\rho s)(\alpha_\rho(t)-1)} \quad (33)$$

where $G_{\rho NN} = 3.4$ and $\kappa_\rho = 6.1$ are the standard vector and anomalous tensor coupling constants, respectively. The ρ-trajectory adopted here reads $\alpha_\rho(t) = 0.53 + \alpha'_\rho t$ with a slope $\alpha'_\rho = 0.85$ GeV^{-2}. The Γ function in (33) contains the pole propagator $\sim 1/\sin(\pi\alpha_\rho(t))$ but no zeroes and the amplitude zeroes only occur through the factor $1 - e^{-i\pi\alpha_\rho(t)}$.

The $\rho\gamma\pi$ coupling constants $G_{\rho\gamma\pi}$ can be deduced from the radiative $\gamma\pi$ decay widths of ρ

$$\Gamma(\rho^\pm \to \gamma\pi^\pm) = \frac{\alpha_e}{24} \frac{G^2_{\rho\gamma\pi}}{m^3_\rho} \left(m^2_\rho - m^2_\pi\right)^3 . \quad (34)$$

The measured width [46]: $\Gamma_{\rho^\pm\to\gamma\pi^\pm} = (68 \pm 7)$ keV, where the central value corresponds to $G_{\rho\gamma\pi} = 0.728$ GeV^{-1}. For the transition form factor $F_{\rho\gamma\pi}(Q^2)$ we use a VMD model $F_{\rho\gamma\pi}(Q^2) = (1 + Q^2/\Lambda^2_{\rho\gamma\pi})^{-1}$ with $\Lambda_{\rho\gamma\pi} = m_{\omega(782)}$.

B. Axial-vector $I^G(J^{PC}) = 1^-(1^{++})$ exchange currents

The axial-vector $a_1(1260)$ meson with $I^G(J^{PC}) = 1^-(1^{++})$ has a large width into the $a_1(1260)^\pm \to \gamma\pi^\pm$ channel [46]. A conversion of a_1 into $\gamma\pi$ is described by the $a_1\gamma\pi$ vertex $\mathcal{L}_{a_1\gamma\pi} = \frac{-ie}{4} G_{a_1\gamma\pi} F^{\mu\nu} \langle Q[A_{\mu\nu}, \varphi]\rangle$ where $F^{\mu\nu}$ denotes the field tensor of photons, $A_{\mu\nu}$ stands for the field tensor of the axial-vector meson with $A_{\mu\nu} = \partial_\mu A_\nu - \partial_\nu A_\mu$ and

$$A_\mu = \begin{pmatrix} a^0_1 & \sqrt{2}a^+_1 \\ \sqrt{2}a^-_1 & -a^0_1 \end{pmatrix}_\mu . \quad (35)$$

φ is a standard $SU(2)$ pion matrix, $Q = \mathrm{diag}(2/3, -1/3)$ is a quark charge matrix, $\langle..\rangle$ and $[..]$ denote a trace and a commutator of fields. The hadronic a_1NN interaction is described by

$$\mathcal{L}_{a_1NN} = G_{a_1NN} \bar{\psi}\gamma^\mu\gamma_5 A_\mu \psi, \quad (36)$$

where $\psi = (p, n)^{\mathrm{T}}$. Because of G-parity conservation in the vertex there is no tensor coupling of a_1 to nucleons.

In the reactions $p(\gamma^*,\pi^+)n$ and $n(\gamma^*,\pi^-)p$ the currents describing the exchange of $a_1(1260)$ trajectory read

$$\left[\begin{array}{c} -iJ^\mu_{a_1}(\gamma^* p\to\pi^+ n) \\ -iJ^\mu_{a_1}(\gamma^* n\to\pi^- p)\end{array}\right] = \left[\begin{array}{c} + \\ - \end{array}\right]\sqrt{2}\,G_{a_1 NN}G_{a_1\gamma\pi}F_{a_1\gamma\pi}(Q)\Big[k^\mu q^\nu-(qk)g^{\mu\nu}\Big]\bar{u}_{s'}(p')\gamma_\nu\gamma_5 u_s(p)$$
$$\times\left[\frac{1-e^{-i\pi\alpha_{a_1}(t)}}{2}\right]\left(-\alpha'_{a_1}\right)\Gamma[1-\alpha_{a_1}(t)]e^{\ln(\alpha'_{a_1}s)(\alpha_{a_1}(t)-1)}, \tag{37}$$

The a_1 Regge trajectory adopted here is $\alpha_{a_1}(t)=\alpha_\rho(t)-1$ where $\alpha_\rho(t)$ is the trajectory of ρ. The $\gamma^*\to a_1\pi$ transition is isovector and contributes with opposite signs to $\gamma^*p\to\pi^+n$ and $\gamma^*n\to\pi^-p$ reactions.

To estimate the a_1-nucleon coupling constant G_{a_1NN} one can relate say G_{a_1pp} to the observed axial-vector coupling constant using axial-vector dominance [47, 48] $\frac{g_A}{g_V}=\frac{\sqrt{2}f_{a_1}G_{a_1pp}}{m^2_{a_1}}$, where the weak decay constant f_{a_1} is deduced from τ decay: $\tau\to a_1+\nu_\tau$. With $g_A/g_V=1.267$, $f_{a_1}=(0.19\pm0.03)$ GeV^2 one gets the following estimate $G_{a_1pp}=G_{a_1NN}=7.1\pm1.0$.

The radiative decay width $a_1\to\gamma\pi$ is given by

$$\Gamma_{a_1^+\to\gamma\pi^+}=\frac{\alpha_e}{24}\frac{G^2_{a_1\gamma\pi}}{m^3_{a_1}}(m^2_{a_1}-m^2_\pi)^3, \tag{38}$$

The empirical width $a_1^+\to\gamma\pi^+$ is $\Gamma_{a_1^+\to\gamma\pi^+}\simeq(640\pm246)$ keV [46]. The coupling constant $G_{a_1\gamma\pi}\simeq1.1$ GeV^{-1} corresponds to the central value. In a VMD picture a conversion of γ to ρ with subsequent $a_1\rho\pi$ interaction generates the monopole form factor $F_{a_1\gamma\pi}(Q^2)=(1+Q^2/\Lambda^2_{a_1\gamma\pi})^{-1}$ with $\Lambda_{a_1\gamma\pi}=m_{\rho(770)}$. This form is used to model the Q^2 dependence of the $a_1\gamma^*\pi$ vertex.

C. Axial-vector $I^G(J^{PC})=1^+(1^{+-})$ exchange currents

We consider the exchange of $b_1(1235)$ axial-vector meson with $I^G(J^{PC})=1^+(1^{+-})$. The conversion of $b_1\to\gamma\pi$ is described by the vertex $\mathcal{L}_{b_1\gamma\pi}=\frac{eG_{b_1\gamma\pi}}{4}F^{\mu\nu}\langle Q\{B_{\mu\nu},\varphi\}\rangle$, where $\{..\}$ anti-commutes and $B_{\mu\nu}=\partial_\mu B_\nu-\partial_\nu B_\mu$ with

$$B_\mu=\left(\begin{array}{cc} b_1^0 & \sqrt{2}b_1^+ \\ \sqrt{2}b_1^- & -b_1^0\end{array}\right)_\mu. \tag{39}$$

The $b_1(1235)$ coupling to nucleons takes the form of axial-tensor interaction

$$\mathcal{L}_{b_1NN} \;=\; i\frac{G_{b_1NN}}{4M_N}\,\bar{\psi}\sigma^{\mu\nu}\gamma_5 B_{\mu\nu}\psi. \tag{40}$$

where $\sigma^{\mu\nu}=\frac{i}{2}[\gamma^\mu,\gamma^\nu]$. The hadronic currents $-iJ^\mu_{b_1}$ describing the exchange of $b_1(1235)$ Regge trajectory read

$$\left[\begin{array}{c} -iJ^\mu_{b_1}(\gamma^* p\to\pi^+ n) \\ -iJ^\mu_{b_1}(\gamma^* n\to\pi^- p)\end{array}\right] \;=\; \frac{\sqrt{2}}{3}\,\frac{G_{b_1NN}}{2M_N}G_{b_1\gamma\pi}F_{b_1\gamma\pi}(Q)\Big[k^\mu q^\nu-(qk)g^{\mu\nu}\Big](p+p')_\nu\bar{u}_{s'}(p')\gamma_5 u_s(p)$$
$$\times\;\left[\frac{1-e^{-i\pi\alpha_{b_1}(t)}}{2}\right]\left(-\alpha'_{b_1}\right)\Gamma[1-\alpha_{b_1}(t)]e^{\ln(\alpha'_{b_1}s)(\alpha_{b_1}(t)-1)}. \tag{41}$$

The radiative decay width of $b_1^\pm\to\gamma\pi^\pm$ is $\Gamma_{b_1^\pm\to\gamma\pi^\pm}=(230\pm60)$ keV [46]. Making use of an expression similar to Eq. (38) one gets $G_{b_1\gamma\pi}/3=0.647$ GeV^{-1}. The π and $b_1(1235)$ Regge trajectories are nearly degenerate (dashed curve if Figure 3). Therefore we assume $\alpha_{b_1}(t)=\alpha_\pi(t)$. In the $b_1\gamma^*\pi$ vertex we use the VMD form factor $F_{b_1\gamma\pi}(Q^2)=(1+Q^2/\Lambda^2_{b_1\gamma\pi})^{-1}$ with $\Lambda_{b_1\gamma\pi}=m_{\omega(782)}$.

It was proposed [29] that the polarized photon asymmetry in $p(\gamma,\pi^0)p$ reaction at high energies can be used to estimate the product of the b_1 electromagnetic and strong coupling constants. In [29] the $b_1^0(1235)$ is coupled to the axial-vector current and the axial-tensor interaction has been neglected. However, the axial-vector

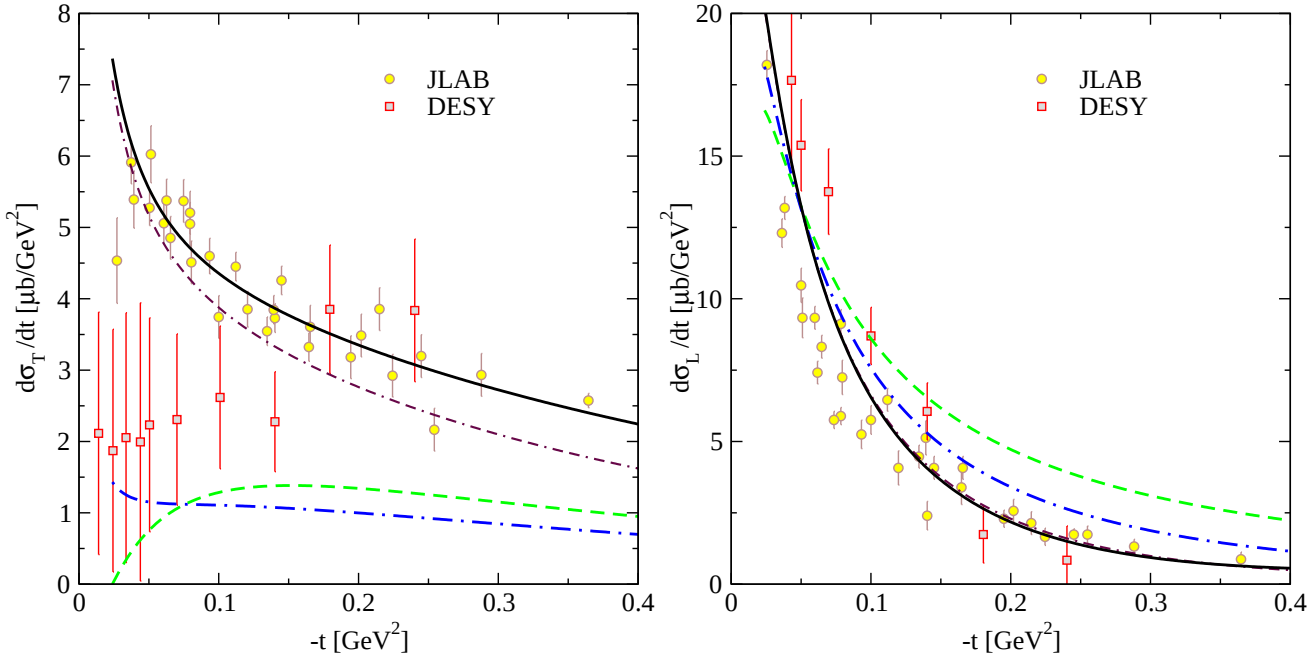

FIG. 4: (Color online) $-t$ dependence of the transverse $d\sigma_T/dt$ (left panel) and longitudinal $d\sigma_L/dt$ (right panel) differential cross sections in exclusive reaction $p(\gamma^*,\pi^+)n$. The compilation of JLAB and old DESY data are from Ref. [4] and have been scaled to common values of $W = 2.19$ GeV and $Q^2 = 0.7$ GeV^2. The solid curves describe the model results which include the effect of resonances and exchange of $\pi/b_1(1235)$, $\rho(770)/a_2(1320)$ and $a_1(1260)$ Regge trajectories. The same is true for the dash-dash-dotted curves but without the DIS slope of Eq. (45). The dashed curves correspond to the contribution of the π-reggeon exchange only. The dash-dotted curves describe the model results which include the exchange of Regge trajectories and on-mass-shell parameterization of the proton Dirac form factor.

$\gamma^\mu\gamma_5$ vertex is C-parity even and can not couple to the $b_1^0(1235)$-meson which has negative C-parity. This is opposed to the $a_1(1260)$ which couples to $\gamma^\mu\gamma_5$. By $C(G)$-parity only a tensor b_1NN coupling, Eq. (40), is possible. We have checked and found that with the proper b_1NN vertex this extraction is not obvious. With the tensor interaction the exchange of the $b_1(1235)$ trajectory is negligibly small and can be readily neglected. For instance, using $G_{b_1NN} = G_{a_1NN}$ or even increasing considerably the latter value does not produce any noticeable effects on the observables considered here.

VI. ELECTROPRODUCTION ABOVE THE RESONANCE REGION

In this section we demonstrate the resonance interpretation proposed in this work and fix the model parameters using the JLAB data. At first, we briefly consider the real photon limit of the Regge amplitudes at high energies. In π^+ and π^- photoproduction at very forward angles the reggeized electric amplitudes, see Eqs. (9) and (10), are supposed to be dominant. Since the vector and axial-vector meson-exchange contributions vanish at forward angles, Eqs. (9) and (10) are parameter free, provided the intercept of the π-trajectory and the $g_{\pi NN}$ coupling constant are fixed. However, further assumptions concerning a choice of the phases in the Regge amplitudes have to be made. In the gauged π-Regge amplitudes, Eqs. (9) and (10), an assumption concerning an exact degeneracy of π and axial-vector $b_1(1235)$ Regge trajectories with a choice of rotating phase in π^+ and a constant phase in π^- photoproduction yields a remarkable consistency with data [29]. The degeneracy of $\rho(770)/a_2(1320)$ Regge trajectories and G-parity arguments result in a rotating phase in π^+ and a constant phase in π^- production described by the ρ-exchange amplitude, Eq. (33). Here, to be consistent with the real photon limit, we follow these assumptions [29]. However, in the high-Q^2 electroproduction a particular choice of phases in the Regge amplitudes is of minor importance. The virtual photon $(\gamma^*,\pi^\pm)$ results presented here can be well reproduced with the standard Regge propagators. From the meson spectrum there is no conclusive evidence that a leading Regge trajectory for an unnatural parity ρ_2 state exists. Therefore, we do not make any assumptions on a degeneracy pattern of $a_1(1260)$.

The resulting Regge model based on reggeized gauge invariant Feynman amplitudes describes the high energy $\pi^\pm$ photoproduction data relevant for the present studies reasonably well. These include the differential cross sections above the resonance region, the π^-/π^+ ratio of the $n(\gamma,\pi^-)p$ and $p(\gamma,\pi^+)n$ differential cross sections and polarized photon asymmetries. Our description of photoproduction data is quantitatively similar to the results of Ref. [29] and we do not repeat this comparison with

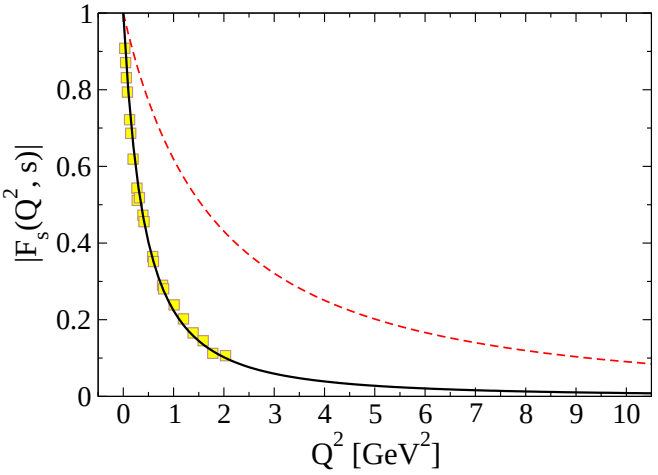

FIG. 5: (Color online) The Q^2 dependence of the absolute value of the transition form factor $|F_s(Q^2,s)|$ (dashed curve), Eq. (43), at $\sqrt{s} = 2.2$ GeV. The solid curve describes the proton Dirac form factor, Eq (42), in comparison with data.

experimental data here.

An extension of the model to electroproduction is straightforward provided the Q^2-dependent transition form factors are defined. In Figure 4 we plot the transverse $d\sigma_{\rm T}/dt$ (left panel) and longitudinal $d\sigma_{\rm L}/dt$ (right panel) π^+ electroproduction data from JLAB and DESY (old data) scaled to the same values of $Q^2 = 0.7$ GeV^2 and $W = 2.19$ GeV [4]. The value of the momentum cut-off $\Lambda_{\gamma\pi\pi}$ in the pion form factor, Eq. (14), is largely constrained by the magnitude of $d\sigma_{\rm L}/dt$ at forward angles. In the following the JLAB data are considered to be a guideline for fixing the model parameters. The dashed curves correspond to $\Lambda^2_{\gamma\pi\pi} = 0.46$ GeV^2 and describe the contribution of the π-reggeon exchange only. The exchange of π dominates in $d\sigma_{\rm L}/dt$ at forward angles. However, in $d\sigma_{\rm T}/dt$ the π-exchange is not compatible with data and also vanishes in the forward direction. The dash-dotted curves correspond to the gauged electric model with the on-shell Dirac form factor, see Eq. (15),

$$F_1^p(Q^2) = \frac{G_E^p(Q^2)/G_M^p(Q^2) + Q^2/4M_p^2}{1+Q^2/4M_p^2} G_M^p(Q^2), \quad (42)$$

and exchange of $\rho(770)/a_2(1320)$ and $a_1(1260)$ Regge trajectories. In Eq. (42) the electric form factor G_E^p decreases linearly as a function of Q^2 with respect to the magnetic form factor G_M^p with a node around $Q_0^2 \simeq 8$ GeV^2 [49] provided $\mu_p G_E^p/G_M^p = 1 - Q^2/Q_0^2$. On the other hand up to $\simeq 5$ GeV^2 the magnetic form factor is a dipole $G_M^p = \mu_p/(1+Q^2/0.71{\rm GeV}^2)^2$ where $\mu_p = 2.793$ is the magnetic moment of the proton.

As one can see, this model (dash-dotted curves) with the nucleon-pole (gauge invariance), vector and axial-vector meson-exchange Regge trajectories describes $d\sigma_{\rm L}/dt$ well and grossly underestimates $d\sigma_{\rm T}/dt$. Variations of the cut-offs in the vector and axial-vector meson transition form factors do not improve the description. This preliminary comparison with data shows that being consistent with photoproduction the above simple extension of the Regge model to electroproduction is not able to describe the data already at values of Q^2 as low as $Q^2 \simeq 1$ GeV^2. The discrepancies with data increase with increasing value of Q^2 [4].

Next, consider the resonance contributions using the transition form factors as defined in Eq. (31). We have two parameters at hand: the parameter β which is related to the level density of states and a parameter ξ describing the average cut-off in the resonance transition form factors. All the exclusive $p(\gamma^*,\pi^+)n$ and $n(\gamma^*,\pi^-)p$ electroproduction data considered in this work from JLAB, DESY and Cornell to DIS region at HERMES can be well described by the choice $\beta = 3$ and $\xi = 0.4$. The formulae for the transition form factors given in (31) and (32) can be integrated and yield (for $\beta = 3$)

$$F_s(Q^2,s) = \frac{s\ln\left[\frac{\xi Q^2}{M_p^2}+1\right]\frac{(2\xi Q^2+s)}{(\xi Q^2)^2} - \frac{s(\xi Q^2+s)}{\xi Q^2\,(\xi Q^2+M_p^2)} + \ln\left[\frac{s-M_p^2}{M_p^2}\right] - i\pi}{\left(\frac{\xi Q^2}{s}+1\right)^2\left(\frac{s^2+2sM_p^2}{2M_p^4} + \ln\left[\frac{s-M_p^2}{M_p^2}\right] - i\pi\right)}, \quad (43)$$

$$F_u(Q^2,u) = \frac{u\ln\left[\frac{\xi Q^2}{M_p^2}+1\right]\frac{(2\xi Q^2+u)}{(\xi Q^2)^2} - \frac{u(\xi Q^2+u)}{\xi Q^2\,(\xi Q^2+M_p^2)} + \ln\left[\frac{M_p^2-u}{M_p^2}\right]}{\left(\frac{\xi Q^2}{u}+1\right)^2\left(\frac{u^2+2uM_p^2}{2M_p^4} + \ln\left[\frac{M_p^2-u}{M_p^2}\right]\right)}. \quad (44)$$

In Figure 5 we plot the Q^2 dependence of the absolute value of the transition form factor $|F_s(Q^2,s)|$ (dashed

Regge exchange	Parameters	$p(\gamma^*,\pi^+)n$	$n(\gamma^*,\pi^-)p$	Regge trajectory $\alpha_i(t)=\alpha_i^0+\alpha_i' t$
$\pi(140)/b_1(1235)$	$g_{\pi NN}=13.4$	$+e^{-i\pi\alpha_\pi(t)}$	1	$\alpha_\pi(t)=\alpha_\pi'(t-m_\pi^2)$ $\alpha_\pi'=0.74$
$\rho(770)/a_2(1320)$	$G_{\rho NN}=3.4$ $\kappa_\rho=6.1$ $G_{\rho\gamma\pi}=0.728$ GeV^{-1} $\Lambda_{\rho\gamma\pi}=m_{\omega(782)}$	$-e^{-i\pi\alpha_\rho(t)}$	1	$\alpha_\rho(t)=0.53+0.85t$
$a_1(1260)$	$G_{a_1NN}=7.1$ $G_{a_1\gamma\pi}=1.1$ GeV^{-1} $\Lambda_{a_1\gamma\pi}=m_{\rho(770)}$	$\frac{1-e^{-i\pi\alpha_{a_1}(t)}}{2}$	$\frac{1-e^{-i\pi\alpha_{a_1}(t)}}{2}$	$\alpha_{a_1}(t)=\alpha_\rho(t)-1$
Resonances	$\beta=3$, $\xi=0.4$	$+e^{-i\pi\alpha_\pi(t)}$	1	$\alpha_\pi(t)$ with $\alpha_\pi'\to\frac{\alpha_\pi'}{1+a\frac{Q^2}{W^2}}$ $a=2.4$

TABLE I: A summary table of a model parameters. See the text for the details.

curve) at $W=\sqrt{s}=2.2$ GeV in comparison with the on-shell parameterization of the proton's Dirac form factor $F_1^p(Q^2)$ Eq. (42) (solid curve). It is clearly seen that F_s is considerably harder than F_1^p. This difference reflects the influence of the higher lying resonances.

There is an additional effect which we would like to take into account. In Refs. [25, 27] it has been observed that in exclusive reaction $(e,e'\pi^+)$ the slope of partonic contributions which is driven by the intrinsic transverse momentum distribution of partons slightly decreases with increasing value of Q^2. Since in our present description the contribution of resonances is dual to direct partonic interaction we accommodate this anti-shrinkage effect in the transition form factors $\mathcal{F}_{s(u)}$, see Eq. (13), using the slope parameter

$$\alpha_\pi' \to \frac{\alpha_\pi'}{1+a\frac{Q^2}{W^2}}, \tag{45}$$

with $a\simeq 2.4$. This behavior has been found from the fit to the (Q^2,W) dependence of the transverse partonic DIS slope of [25, 27]. Eq. (45) is effective in electroproduction and in the resonance transition form factors $\mathcal{F}_{s(u)}$, Eq. (13), only. For real photons the phase of $\mathcal{F}_{s(u)}$ is that of $\mathcal{F}_{\gamma\pi\pi}$ and a proper Regge limit of [29] is guaranteed.

Then using the R/P-transition form factor, Eq. (43), the transverse cross section $d\sigma_{\rm T}/dt$ gets large (solid curve) in agreement with JLAB data, see Figure 4. The effect of resonances is much smaller in the longitudinal response $d\sigma_{\rm L}/dt$ but it improves the description of data at higher values of $-t$. As we shall see, the same effect will strongly influence the interference cross sections and allow to explain both the sign and magnitude of $d\sigma_{\rm TT}/dt$ and $d\sigma_{\rm LT}/dt$. The solid curves include the effect of the DIS slope, Eq. (45). The dash-dash-dotted curves correspond to the results without Eq. (45); the effect is rather small at forward angles and could be partially absorbed in a redefinition of ξ. To be in line with [25, 27] we keep this phenomenological behavior.

The model parameters are summarized in Table I. The Regge phase pattern discussed above and used in the calculations is also shown for different reggeon exchange contributions. The cut-off $\Lambda_{\gamma\pi\pi}$ in the pion form factor, Eq. (14), is a fit parameter. From the fit to the longitudinal data we observe essentially three regions. At small values of $Q^2<0.4$ GeV^2 the model results are remarkably consistent with a VMD value of $\Lambda^2_{\gamma\pi\pi}=m^2_{\rho(770)}\simeq 0.59$ GeV^2. The intermediate region $0.6<Q^2<1.5$ GeV^2 in $F\pi$-1 experiment [2] demands somewhat smaller value of $\Lambda^2_{\gamma\pi\pi}\simeq 0.4$ GeV^2. In the deep (Q^2,W) region the JLAB, Cornell and DESY data can be well described using $\Lambda^2_{\gamma\pi\pi}\simeq 0.46$ GeV^2. In our calculations we shall follow these prescriptions for $\Lambda_{\gamma\pi\pi}$.

VII. JLAB $F\pi$-1, $F\pi$-2 AND π-CT DATA

In this section we study the R/P-effects in partial π^+ electroproduction cross sections measured at JLAB. We compare the model results with the differential cross sections in the $p(\gamma^*,\pi^+)n$ reaction from the $F\pi$-1 [2], $F\pi$-2 [1] and π-CT [3] experiments. At JLAB the reaction $n(\gamma^*,\pi^-)p$ has been also measured off the deuteron target and π^- data will be soon reported [50].

In Figure 6 we show our results for the $p(\gamma^*,\pi^+)n$ reaction together with the high-Q^2 data from [1, 3]. The data points in each (Q^2,W) bin correspond to slightly different values of Q^2 and W for the various $-t$ bins. The numbers displayed in the plots are the average (Q^2,W) values. For simplicity we perform the calculations for values of (Q^2,W) corresponding to the first $-t$ bin. A proper binning of the curves does not change much the results [25].

At first, we consider again the reggeized π-exchange only. The value of the cut-off in the pion from factor is

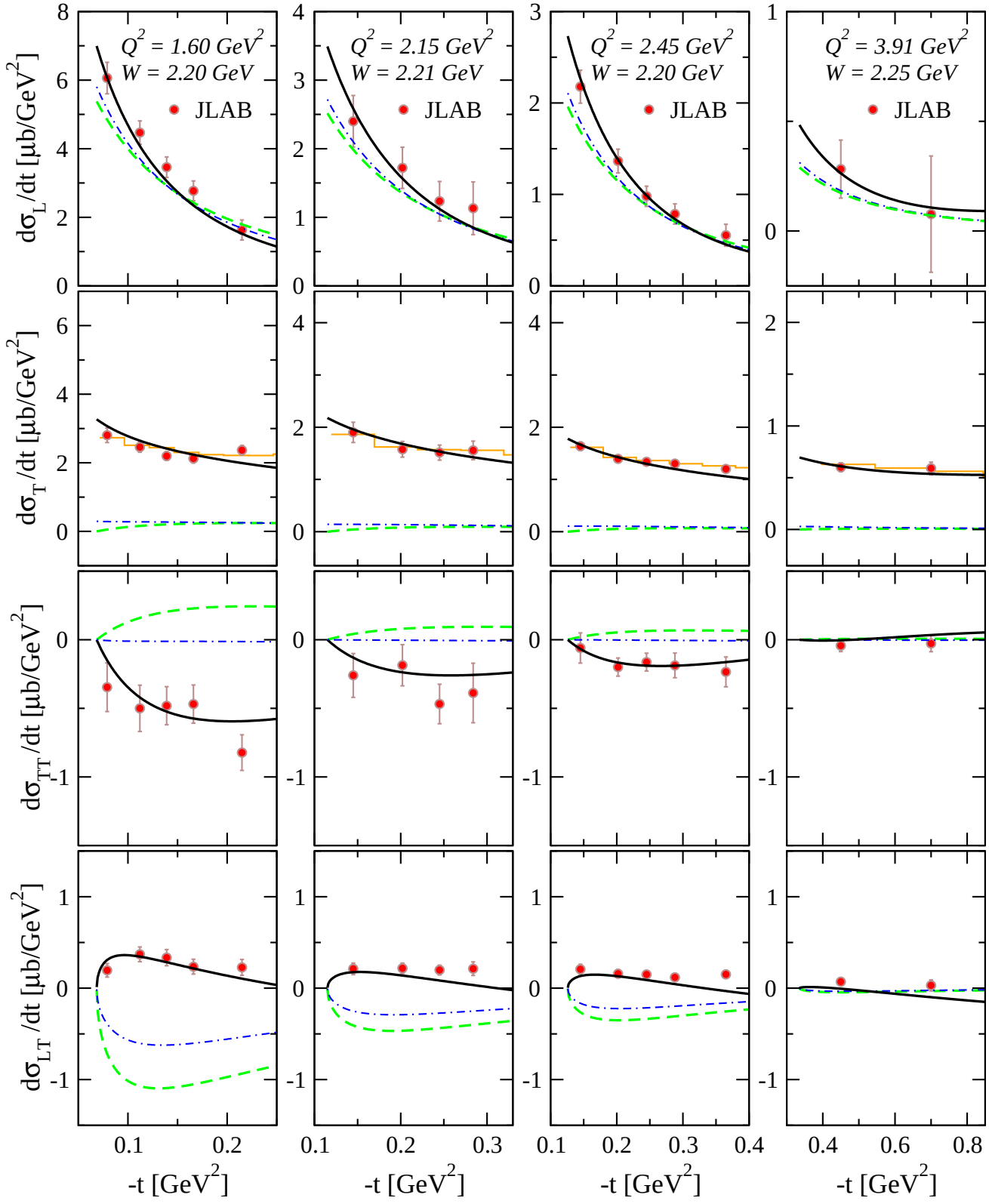

FIG. 6: (Color online) $-t$ dependence of L/T partial transverse $d\sigma_T/dt$, longitudinal $d\sigma_L/dt$ and interference $d\sigma_{TT}/dt$ and $d\sigma_{LT}/dt$ differential cross sections in exclusive reaction $p(\gamma^*,\pi^+)n$. The experimental data are from the $F\pi$-2 [1] and π-CT [3] experiments at JLAB. The numbers displayed in the plots are the average (Q^2, W) values. The dashed curves correspond to the exchange of the π-Regge trajectory alone. The dash-dotted curves are obtained with the on-mass-shell form factors in the nucleon-pole contribution and exchange of the $\rho(770)/a_2(1320)$-trajectory. The solid curves describe the model results with the resonance contributions. The data points in each (Q^2, W) bin correspond to slightly different values of Q^2 and W for the various $-t$ bins. The calculations are performed for values of Q^2 and W corresponding to the first $-t$ bin. The histograms for $d\sigma_T/dt$ are the results from [25].

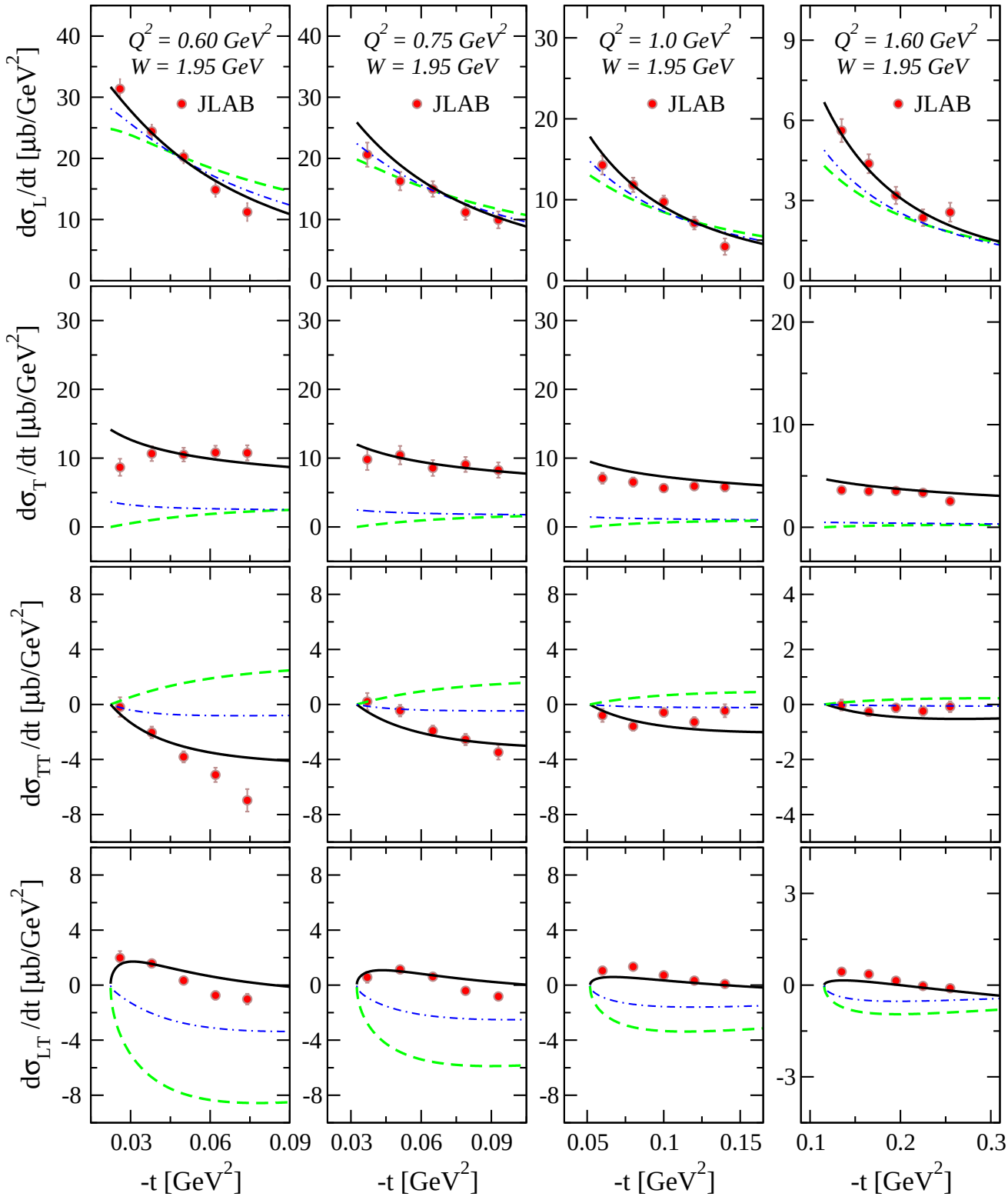

FIG. 7: (Color online) $-t$ dependence of L/T partial differential cross sections in exclusive reaction $p(\gamma^*, \pi^+)n$. The experimental data are from the $F\pi$-1 experiment at JLAB [2]. The notations for the curves are the same as in Figure 6.

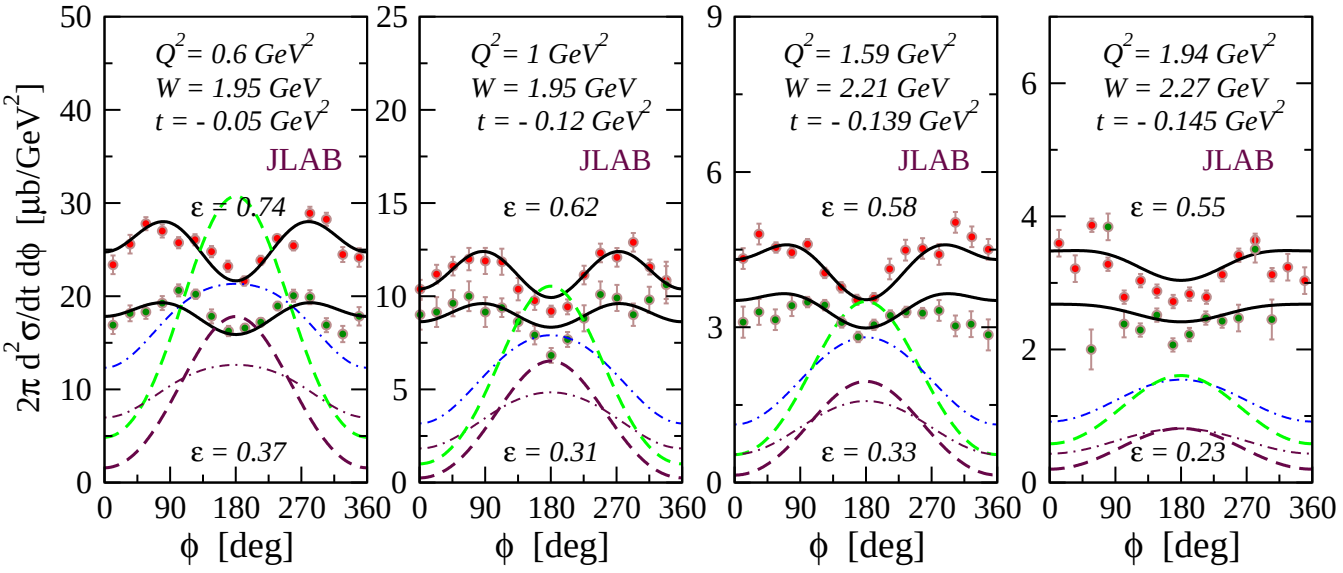

FIG. 8: (Color online) ϕ dependence of the differential cross sections $2\pi\, d^2\sigma/dtd\phi$ in exclusive reaction $p(\gamma^*,\pi^+)n$ at fixed $(-t, Q^2, W)$ and two (high and low) values of ε. The notations for the curves are the same as in Figure 6. The upper set of solid, dashed and dash-dotted curves belong to the higher value of ε. The experimental data are from Refs. [1–3].

$\Lambda^2_{\gamma\pi\pi} = 0.46$ GeV^2. In Figure 6 the dashed curves describe this contribution. As one can see, the steep fall of $d\sigma_{\rm L}/dt$ away from forward angles comes entirely from the rapidly decreasing π-exchange amplitude. The π-exchange practically saturates the longitudinal response $d\sigma_{\rm L}/dt$. At these values of $Q^2 > 1.5$ GeV^2 the contribution of the π-reggeon exchange to the transverse cross section $d\sigma_{\rm T}/dt$ is already marginal. The π-exchange is effective in the interference cross sections. However, experimentally the cross section $d\sigma_{\rm TT}/dt$ is negative and $d\sigma_{\rm LT}/dt$ is positive. The exchange of π contributes here just with opposite signs.

We gauge the π-exchange by adding the nucleon-pole term. The exchanges of $\rho(770)/a_2(1320)$ and $a_1(1260)$ Regge trajectories are also added. This result corresponds to the dash-dotted curves in Figure 6. As one can see, the longitudinal cross sections $d\sigma_{\rm L}/dt$ is barely changed. The transverse cross section $d\sigma_{\rm T}/dt$ is negligibly small but finite at forward angles. The sign of the interference cross section $d\sigma_{\rm TT}/dt$ now respects the experimental data but the magnitude of the cross section is compatible with zero. The cross section $d\sigma_{\rm LT}/dt$ has been increased by about a factor of two but is still largely negative.

In the last step we use the R/P-transition form factor to include the effect of resonances. The solid curves in Figure 6 correspond to this description. As one can see, all the cross sections are now very well described. Furthermore, the magnitude of $d\sigma_{\rm T}/dt$ is strongly correlated with the sign and magnitude of the interference cross sections $d\sigma_{\rm TT}/dt$ and $d\sigma_{\rm LT}/dt$. The description of $d\sigma_{\rm T}/dt$ translates at once into a remarkable description of both interference cross sections. For instance, $d\sigma_{\rm LT}/dt$ changes sign to positive and $d\sigma_{\rm TT}/dt$ gets large and negative. The contribution of resonances to the longitudinal cross section $d\sigma_{\rm L}/dt$ is sizable at forward angles where the pion form factor is extracted [5] and increases with increasing value of Q^2. However, the effect is particularly pronounced in $d\sigma_{\rm T}/dt$ and interference cross sections $d\sigma_{\rm TT}/dt$ and $d\sigma_{\rm LT}/dt$. For instance, at $Q^2 = 2.45$ GeV^2 and $Q^2 = 3.91$ GeV^2 $d\sigma_{\rm T}/dt$ has been increased by about two orders of magnitude.

The histograms in Figure 6 for $d\sigma_{\rm T}/dt$ are from [25]. The assumption used in Ref. [25] for $\gamma^* p \to \pi^+ n$ is that at the invariant masses reached at JLAB nucleon resonances can contribute to the 1π channel as well. Then similar to the use of Regge trajectories in the t-channel that takes higher meson excitations into account one has to consider the direct hard interaction of virtual photons with partons (DIS) since DIS involves all possible transitions of the nucleon from its ground state to any excited state [51]. Modeling the resonance contributions by DIS like processes, followed by hadronization into the $\pi^+ n$ channel, result in histograms shown in Figure 6. Our present treatment of resonance contributions produces a result which is very close to that obtained in our previous work [25]. However, the present approach goes beyond the two-component hadron-parton model of Ref. [25] and allows to study the interference and non-π-pole background effects on the amplitude level.

The transverse $d\sigma_{\rm T}/dt$ component is insensitive to the variation of the cut-off in the pion form factor $\Lambda_{\gamma\pi\pi}$. On the contrary, the magnitude of $d\sigma_{\rm L}/dt$ is driven by this parameter. In Figure 7 we compare the model results with data measured at lower values of (Q^2, W) in the $F\pi$-1 experiment [2]. The calculations are per-

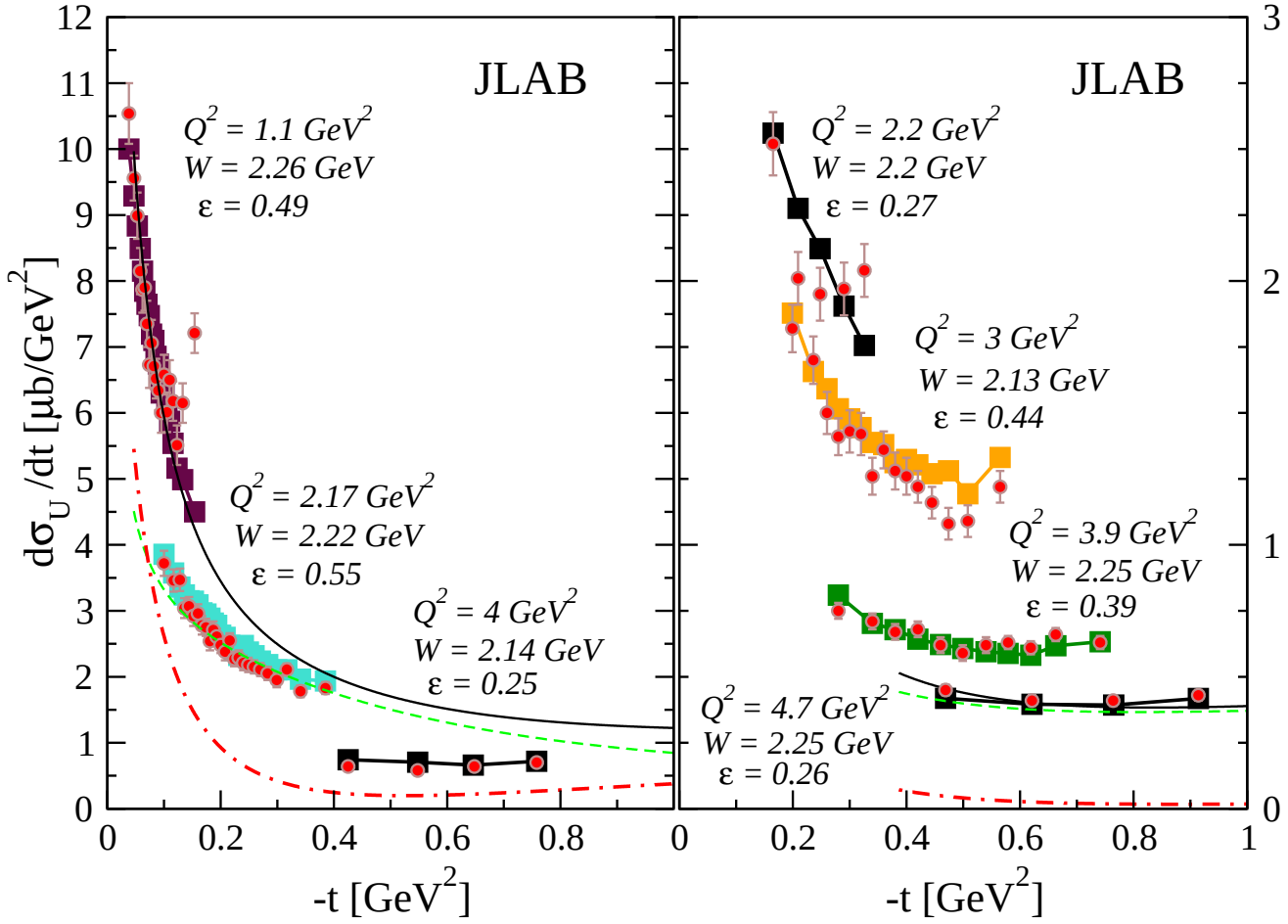

FIG. 9: (Color online) The differential cross sections $d\sigma_U/dt = d\sigma_T/dt + \varepsilon d\sigma_L/dt$ in exclusive reaction $p(\gamma^*,\pi^+)n$ in the kinematics of the π-CT experiment at JLAB [52]. The square symbols connected by solid lines describe the model results. The discontinuities in the curves result from the different values of (Q^2, W, ε) for the various $-t$ bins. The dash-dotted and dashed curves describe the contributions of the longitudinal $\varepsilon d\sigma_L$ and transverse $d\sigma_T$ cross sections, respectively, to the total unseparated cross sections (solid curves) for the the lowest and highest average values of $Q^2 = 1.1$ GeV^2 and $Q^2 = 4.7$ GeV^2.

formed for values of (Q^2, W) corresponding to the first $-t$ bin [2, 4]. The notations for the curves are the same as in Figure 6. In these calculations we used the value of $\Lambda^2_{\gamma\pi\pi} = 0.4$ GeV^2. Also here we find a pronounced resonance contribution in $d\sigma_T/dt$, $d\sigma_{TT}/dt$ and $d\sigma_{LT}/dt$. The slope and magnitude of $d\sigma_L/dt$ at forward angles are also affected by the resonances.

An extraction of L/T partial differential cross sections requires besides the Rosenbluth separation a fit of different harmonics in the azimuthal ϕ-angle distribution of the measured unseparated double differential cross sections. In the actual experiment one measures $d^2\sigma/dtd\phi$ for two different ε bins. In Figure 8 we show the ϕ dependence of $2\pi d^2\sigma/dtd\phi$ in the reaction $p(\gamma^*,\pi^+)n$ at fixed $-t$ and two (high and low) values of ε. This is a representative example of ϕ-dependent exclusive cross sections. In Figure 8 the solid curves are the model results and experimental data are from [1–3]. As in Figures 6 the dashed curves correspond to the contribution of the π-exchange and dash-dotted curves do not account for the resonances. The upper set of solid, dashed and dash-dotted curves belongs to the higher value of ε.

In Figure 9 we confront the result of our calculations with the new JLAB $p(\gamma^*,\pi^+)n$ data [52] for unseparated cross sections $d\sigma_U/dt$, see Eq. (6), at values of $W \simeq 2.2 \div 2.4$ GeV and for different values of (Q^2, ε) bins. The square symbols connected by solid lines describe the model results. The discontinuities in the curves result from the different values of (Q^2, W, ε) for the various $-t$ bins. The data are very well reproduced by the present model in the measured Q^2 range from $Q^2 \simeq 1$ GeV^2 up to 5 GeV^2. In Figure 9 we also show the contributions of the longitudinal $\varepsilon d\sigma_L$ (dash-dotted curves) and transverse $d\sigma_T$ (dashed curves) cross sections to the total unseparated cross sections (solid curves) for the lowest and highest average values of $Q^2 = 1.1$ GeV^2 and $Q^2 = 4.7$ GeV^2. The cross sections at high values of Q^2 are flat and totally transverse. At forward angles a strong

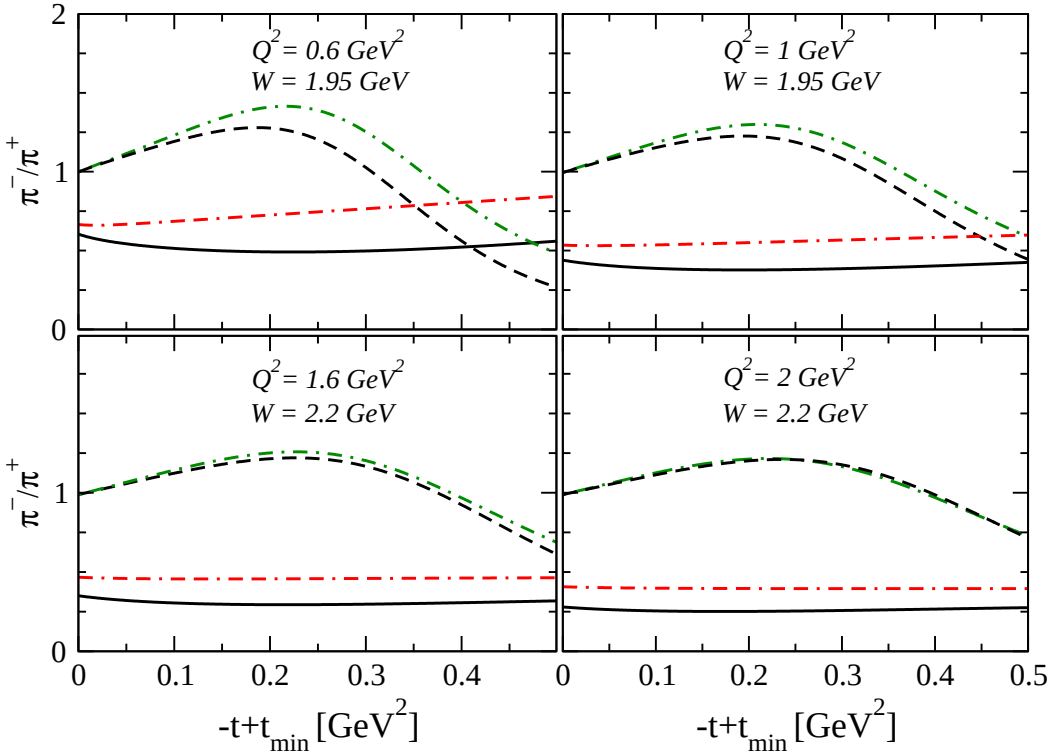

FIG. 10: (Color online) $-t+t_{min}$ dependence of the ratio of longitudinal $R_{\rm L}=d\sigma_{\rm L}^{\pi^-}/d\sigma_{\rm L}^{\pi^+}$ (dashed curves) and transverse $R_{\rm T}=d\sigma_{\rm T}^{\pi^-}/d\sigma_{\rm T}^{\pi^+}$ (solid curves) differential cross sections, $n(\gamma^*,\pi^-)p/p(\gamma^*,\pi^+)n$, for different values of (Q^2,W) at JLAB@5. The dash-dash-dotted and the dash-dotted curves describe $R_{\rm T}$ and $R_{\rm L}$, respectively, without ρ-reggeon exchange.

peaking of the cross section at $Q^2=1.1$ GeV^2 comes from the large longitudinal component in this case. The off-forward region is transverse. This behavior agrees with the results from [25]. As we shall see, the same behavior is observed in the DIS regime at HERMES [7] where the value of W is higher. At HERMES, because of the Regge shrinkage of the π-reggeon exchange and smaller transverse component, the forward peak just has a steeper $-t$-dependence [27].

We now turn to π^- production at JLAB. In [25] the transverse response $d\sigma_{\rm T}/dt$ in the exclusive reaction $n(\gamma^*,\pi^-)p$ was found to be smaller than in the reaction $p(\gamma^*,\pi^+)n$. The present results for the π^- channel are parameter free. The u-channel transition form factors, Eq. (44), entering $n(\gamma^*,\pi^-)p$ have different behavior, since, contrary to the s-channel form factors which depend on (s,Q^2) now they depend on u and Q^2 with

$$u=-s+2M_p^2-t+M_\pi^2-Q^2. \qquad (46)$$

Here we calculate the ratio of π^-/π^+ partial cross sections which is of present interest in the dedicated experiments at JLAB [50]. In Figure 10 we show the results for the ratio of longitudinal $R_{\rm L}=d\sigma_{\rm L}^{\pi^-}/d\sigma_{\rm L}^{\pi^+}$ (dashed curves) and transverse $R_{\rm T}=d\sigma_{\rm T}^{\pi^-}/d\sigma_{\rm T}^{\pi^+}$ (solid curves) cross sections as a function of $-t+t_{min}$, where $-t_{min}$ denotes the minimum value of $-t$ for a given Q^2 and W. The curves have been calculated for the values of $W=1.95$ GeV (top panels) and $W=2.2$ GeV (bottom panels). The values of Q^2 vary from $Q^2=0.6$ GeV^2 (left top) and $Q^2=1$ GeV^2 (right top) to $Q^2=1.6$ GeV^2 (left bottom) and $Q^2=2$ GeV^2 (right bottom). At forward angles the longitudinal ratio $R_{\rm L}$ is close to unity and shows a slow increase followed by a decrease at higher values of $-t$. On the contrary, the ratio $R_{\rm T}$ is practically constant. For $Q^2=0.6$ GeV^2 it is around $R_{\rm T}\simeq 0.6$. With increasing value of Q^2 the ratio $R_{\rm T}$ tends to decrease further and at $Q^2=2$ GeV^2 it gets $R_{\rm T}\simeq 0.26$.

An important mechanism which contributes to the π^-/π^+ asymmetry is an exchange of the ρ-trajectory. It is destructive in π^- and constructive in π^+ channels, respectively. In Figure 10 the dash-dotted (longitudinal ratio) and dash-dash-dotted curves (transverse ratio) correspond to the results without the exchange of ρ. We conclude that $d\sigma_{\rm T}/dt$ in the π^- channel is much smaller than in the π^+ production. Also the interference cross sections follow this behavior since smaller transverse strength translates into smaller $d\sigma_{\rm TT}/dt$ and $d\sigma_{\rm LT}/dt$.

VIII. $p(\gamma^*,\pi^+)n$ AND $n(\gamma^*,\pi^-)p$ AT DESY

The early DESY data [13–16] and [12] provide an access to the $p(\gamma^*,\pi^+)n$ and $n(\gamma^*,\pi^-)p$ reactions cross sec-

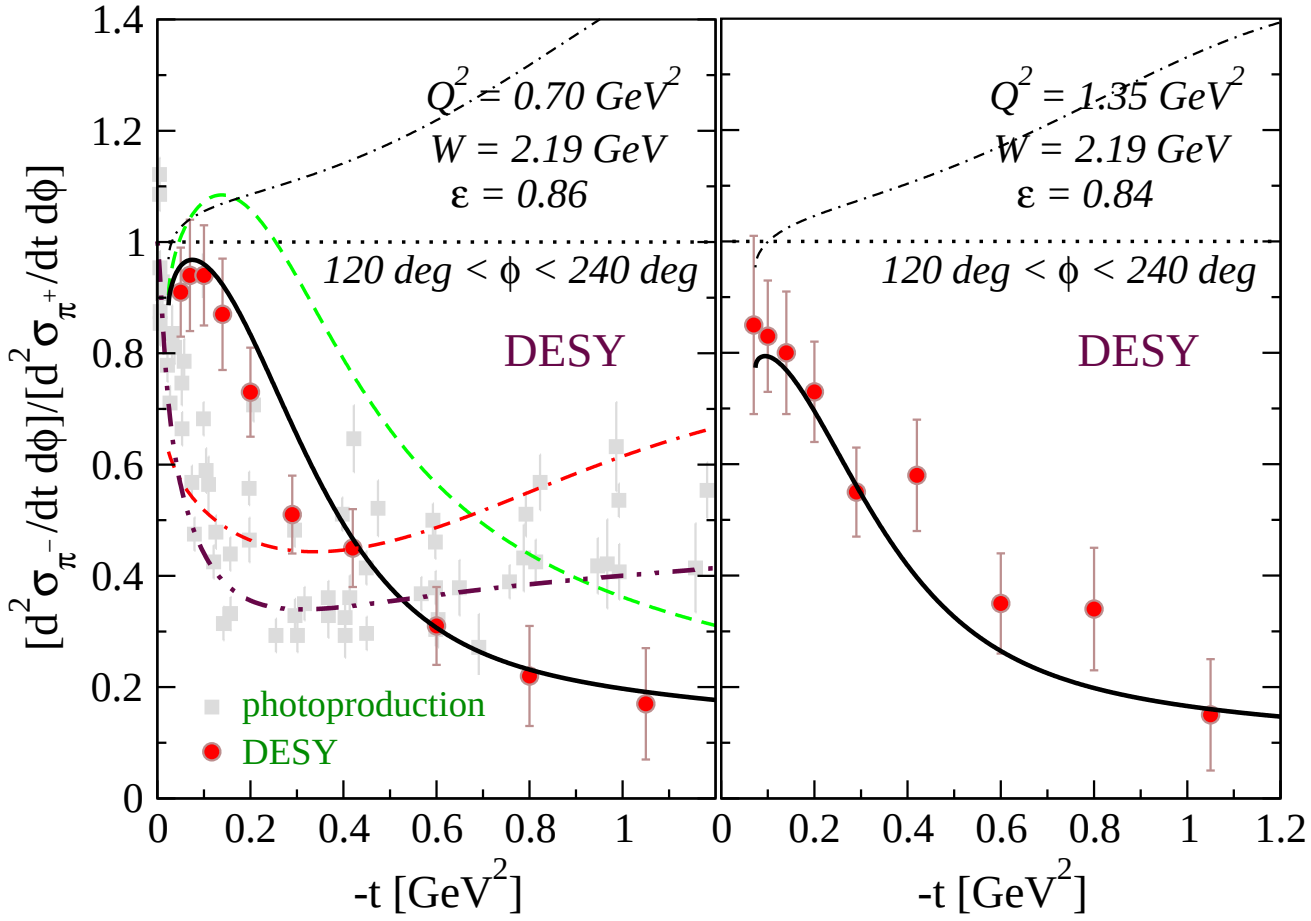

FIG. 11: (Color online) $-t$ dependence of the π^-/π^+ ratio of double differential cross sections $d\sigma^2/dtd\phi$ for the value of $W = 2.19$ GeV and at values of $Q^2 = 0.7$ GeV^2, $\varepsilon = 0.86$ (left panel) and $Q^2 = 1.35$ GeV^2, $\varepsilon = 0.84$ (right panel). The experimental data are from Ref. [16]. The cross sections are integrated in the range of $120^\circ < \phi < 240^\circ$ out-of-plane angles. The solid curves are the model results. The dash-dotted curves describe the results without the resonance contributions. In the left panel the dashed curve is the results without the exchange of the $\rho(770)/a_2(1320)$-trajectory. The squares are the compilation of experimental data for the ratio of π^-/π^+ in photoproduction [55]. The dot-dot-dashed curve corresponds to the ratio of cross sections in photoproduction at $Q^2 = 0$ and $E_\gamma = 16$ GeV. The ratio of transverse cross sections at value of $Q^2 = 0.7$ GeV^2 is given by the dash-dash-dotted curve.

tions in essentially the same (Q^2, W) region as at JLAB. For the proper comparison with data some differences in the conventions used by the two different groups [13–16] and [12] have to be taken into account. The ϕ convention used here follows Refs. [13–16]. In [12] the azimuthal angle is related to that in [13–16] by $\phi \to \pi - \phi$. The latter results in different signs of the measured interference cross section $d\sigma_{\rm LT}/dt$.

In Figure 11 we show the results and the experimental data [16] for the ratio of exclusive π^-/π^+ double differential cross sections $d\sigma^2/dtd\phi$ at the average value of $W = 2.19$ GeV and for the average values of $Q^2 = 0.7$ GeV^2, $\varepsilon = 0.86$ (left panel) and $Q^2 = 1.35$ GeV^2, $\varepsilon = 0.84$ (right panel). The cross sections are integrated in the $120^\circ < \phi < 240^\circ$ azimuthal degree range [16]. The solid curves are the model results. Since, the parameters of the model are constrained using the JLAB $p(\gamma^*, \pi^+)n$ data only, this agreement with data for the ratio $p(\gamma^*, \pi^+)n/n(\gamma^*, \pi^-)p$ of cross sections is indeed remarkable, see the discussion around Eq. (46). In Figure 11 (left panel) the dashed curves are the results without the exchange of the $\rho(770)/a_2(1320)$-Regge trajectory. It is seen that the π^-/π^+ ratio is indeed sensitive to the ρ-exchange amplitude. In the left panel we also show the compilation of experimental data for the ratio of π^-/π^+ photoproduction cross sections at high energies [55]. For comparison we also show the ratio of only the transverse cross sections in electroproduction at $Q^2 = 0.7$ GeV^2 (dash-dash-dotted curve).

The dot-dot-dashed curve in Figure 11 (left panel) corresponds to our results for the ratio of photoproduction ($Q^2 = 0$) cross sections at $E_\gamma = 16$ GeV in the laboratory. The π^-/π^+ asymmetry seen in the photoproduction results mainly from the contribution of the ρ-Regge tra-

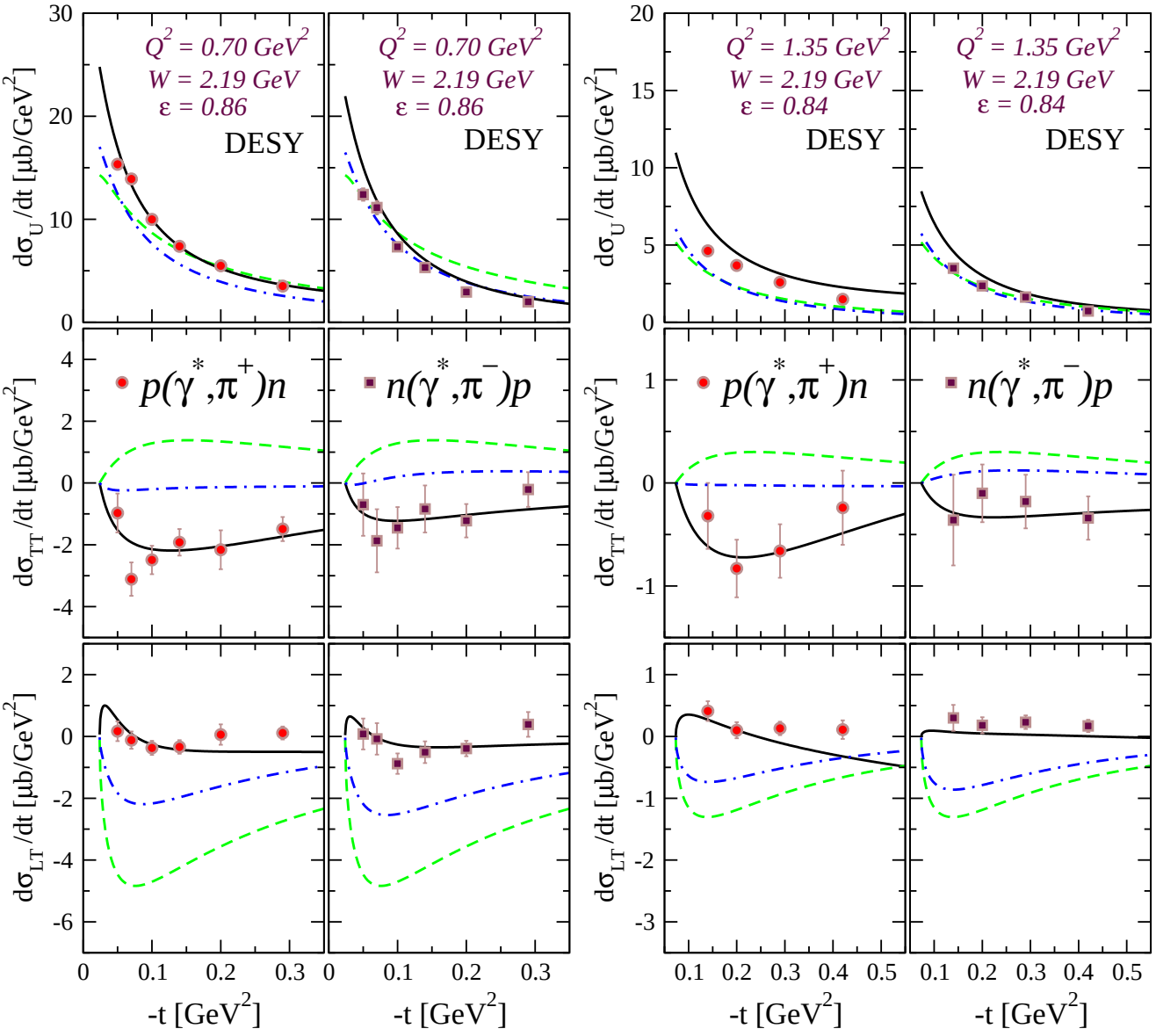

FIG. 12: (Color online) The differential cross sections $d\sigma_{\rm U}/dt = d\sigma_{\rm T}/dt + \varepsilon d\sigma_{\rm T}/dt$ (top), $d\sigma_{\rm TT}/dt$ (middle) and $d\sigma_{\rm LT}/dt$ (bottom) in exclusive reactions $p(\gamma^*,\pi^+)n$ (left panels) and $n(\gamma^*,\pi^-)p$ (right panels) in the kinematics of DESY experiments for the average values of $Q^2 = 0.7$ GeV^2, $W = 2.19$ GeV, $\varepsilon = 0.86$ and $Q^2 = 1.35$ GeV^2, $W = 2.19$ GeV, $\varepsilon = 0.84$. The notations for the curves are the same as in Figure 6. The experimental data are from Ref. [13, 14].

jectory. However, in electroproduction the π^-/π^+ asymmetry is driven by the resonance contributions through the different $(Q^2, s(u))$ dependence of the transition form factors, Eqs. (43) and (44), in the π^+ and π^- channels. For instance, the dash-dotted curves in Figure 11 do not account for the contributions of resonances; the π^-/π^+ ratio is bigger than unity. In the right panel we show the results for the values of $Q^2 = 1.35$ GeV^2 and $\varepsilon = 0.84$.

Our dash-dotted curves which describe the Regge model without the R/P-effects are at variance with the results reported in Ref. [53] where the gauge invariant Regge model with the nucleon-pole contribution has been shown to be in remarkable agreement with the π^-/π^+ electroproduction ratio. This is surprising since the model of [53] is not compatible with the JLAB L/T data in the same (Q^2, W) region [4].

Before drawing definite conclusions concerning these discrepancies, we compare in Figure 12 our model results with the measured differential cross sections $d\sigma_{\rm U}/dt = d\sigma_{\rm T}/dt + \varepsilon d\sigma_{\rm T}/dt$ (top), $d\sigma_{\rm TT}/dt$ (middle) and $d\sigma_{\rm LT}/dt$ (bottom) in exclusive reactions $p(\gamma^*,\pi^+)n$ (left panels) and $n(\gamma^*,\pi^-)p$ (right panels). The experimental data are from Refs. [13, 14]. The average values of (Q^2, W, ε) are the same as in Figure 11 for the π^-/π^+ ratio. The

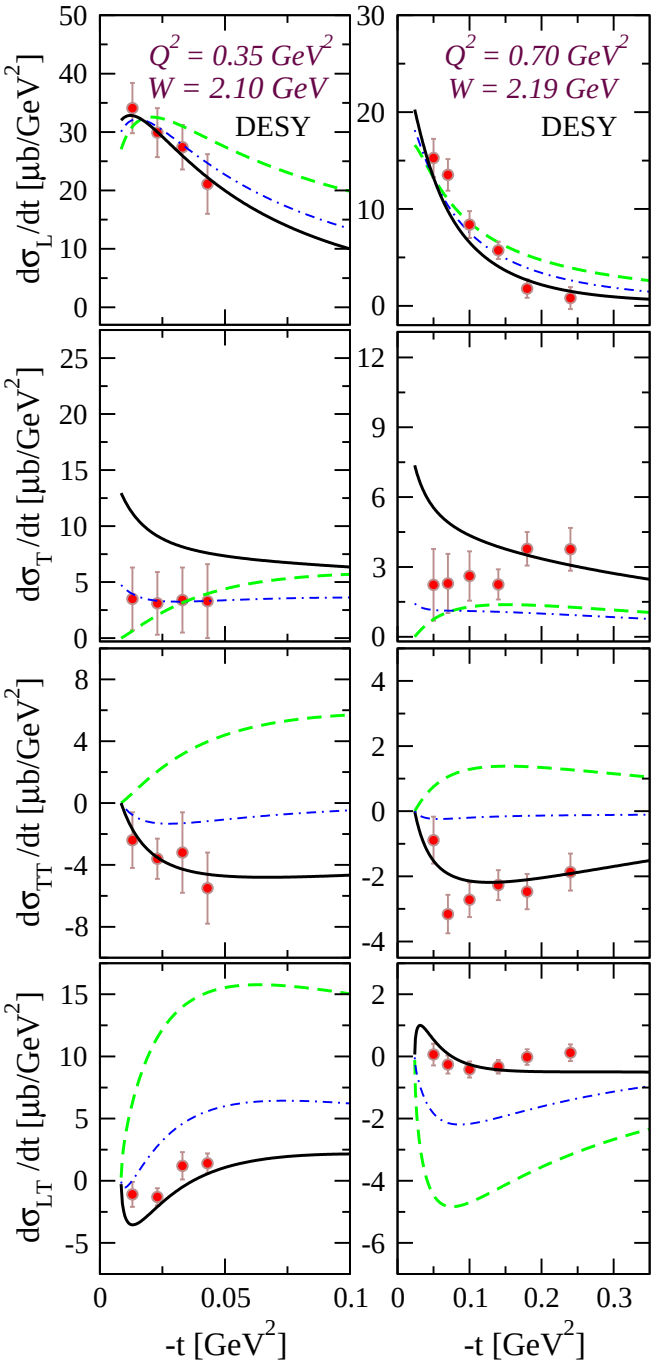

FIG. 13: (Color online) The L/T partial differential cross sections in the reaction $p(\gamma^*,\pi^+)n$ in the kinematics of DESY experiments. The notations for the curves are the same as in Figure 6. The experimental data for values of $Q^2 = 0.35$ GeV^2 are from Ref. [12] and for $Q^2 = 0.7$ GeV^2 are from Ref. [16].

dashed curves which refer to the contribution of the π-exchange are equal in both channels. The solid curves describe the model results and, as one can see, it is not surprising why the π^-/π^+ ratio of double differential cross sections, which involves all four L/T components, is well reproduced. A model without the resonance contributions (dash-dotted curves in Figure 12) fails in both the $p(\gamma^*,\pi^+)n$ and $n(\gamma^*,\pi^-)p$ channels and the behavior of the corresponding results (dash-dotted curves in Figure 11) is expected for the π^-/π^+ ratio.

In Figure 13 (left panel) we compare the results of our calculations with L/T separated $p(\gamma^*,\pi^+)n$ data from [12] with average values of $Q^2 = 0.35$ GeV^2 and $W = 2.1$ GeV. These data are kinematically close to the real photon point where one does not expect a variation of the pion form factor from its VMD value with $\Lambda^2_{\gamma\pi\pi} = m^2_{\rho(770)} \simeq 0.59$ GeV^2. The curves correspond to this choice of $\Lambda_{\gamma\pi\pi}$. In the right panel we also show the L/T separated cross section at $Q^2 = 0.7$ GeV^2 and $W = 2.19$ GeV. The notations for the curves are the same as in Figure 12. As one can notice, because of different conventions for ϕ, the signs of the measured interference cross section $d\sigma_{\rm LT}$ are different for the two data sets.

The interference pattern between the meson-exchange and resonance contributions is different in the π^+ and π^- channels. For π^- production there are no data for the longitudinal and transverse cross sections. However, we conclude that the present model describes rather well the available π^+ and π^- data for the unseparated cross sections $d\sigma_{\rm U}/dt$ and the interference cross sections $d\sigma_{\rm TT}/dt$ and $d\sigma_{\rm LT}/dt$. Concerning the π^-/π^+ ratio, we have seen that the resonance contributions are important and that, contrary to the results of Ref. [53], the model based on reggeon exchanges is not compatible with the observed ratio[1].

IX. DEEPLY VIRTUAL $p(e,e'\pi^+)n$ AT HERMES

The HERMES data at DESY [7] in exclusive reaction $p(e,e'\pi^+)n$ extend the kinematic region to higher values of $W^2 \simeq 16$ GeV^2 toward the DIS region and higher values of $-t$. At HERMES the kinematic requirement $Q^2 > 1$ GeV^2 has been imposed on the scattered electron in order to select the hard scattering regime. The resulting range is $1 < Q^2 < 11$ GeV^2 and $0.02 < x_{\rm B} < 0.55$ for the Bjorken variable. The measured cross sections have been integrated over the azimuthal angle ϕ and a separation of the transverse and longitudinal parts was not feasible. With the 27.6 GeV HERA beam energy the ratio of longitudinal to transverse polarization of the virtual photon ε is close to unity.

The results for the unseparated differential cross sections $d\sigma_{\rm U}/dt = d\sigma_{\rm T}/dt + \varepsilon d\sigma_{\rm L}/dt$ in deeply virtual $p(\gamma^*,\pi^+)n$ reaction at HERMES are shown in Figure 14.

[1] Attempting to resolve the latter discrepancy we assumed that in Figures 2 and 3 of Ref. [53] the convention of Ref. [12] is used for ϕ. This is fine for the data set from [12] in Figures 3 of Ref. [53] but is not correct for the data set from [14] presented in Figures 2 of Ref. [53]. Interestingly, then the π^-/π^+ ratios of Ref. [53] are very well reproduced.

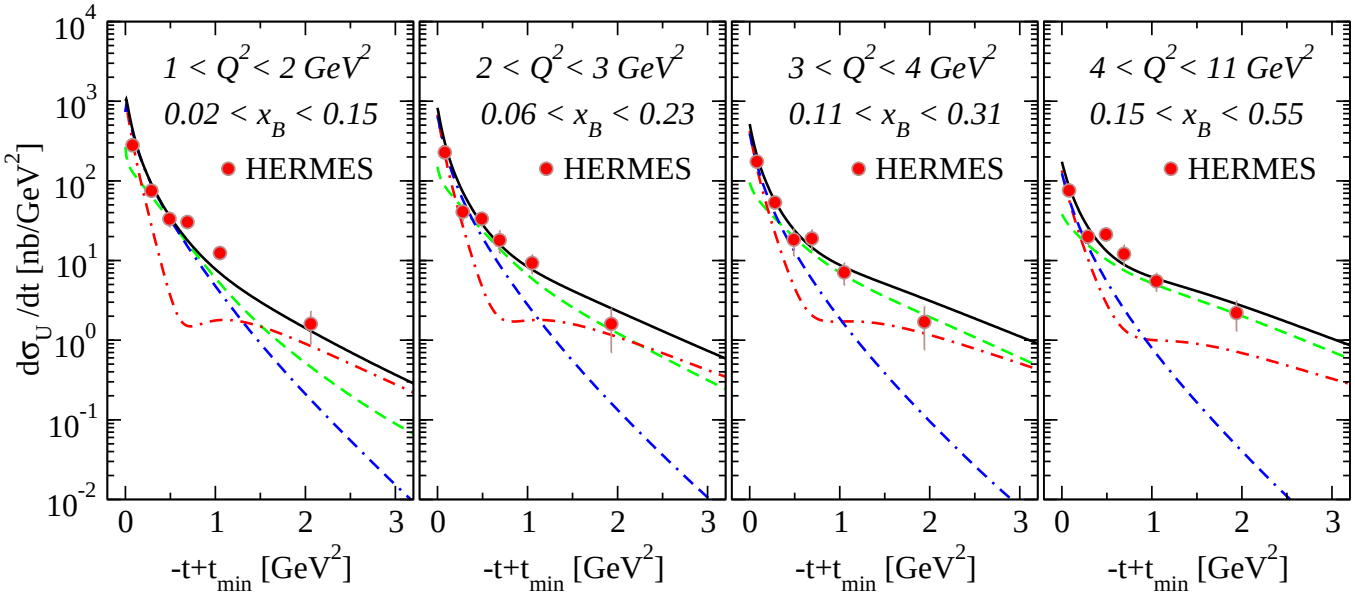

FIG. 14: (Color online) $-t+t_{min}$ dependence of the differential cross section $d\sigma_U/dt = d\sigma_{\rm T}/dt + \epsilon d\sigma_{\rm L}/dt$ in exclusive reaction $p(\gamma^*,\pi^+)n$ at HERMES. The experimental data are from Ref. [7]. The calculations are performed for the average values of $(Q^2, x_{\rm B})$ in a given Q^2 and Bjorken $x_{\rm B}$ bin. The solid curves are the full model results. The dash-dotted curves correspond to the longitudinal $\epsilon d\sigma_{\rm L}/dt$ and the dashed curves to the transverse $d\sigma_{\rm T}/dt$ components of the cross section. The dash-dash-dotted curves describe the results without the resonance/partonic effects.

We perform the calculations for the average (Q^2, x) values in a given Q^2 and $x_{\rm B}$ bin [57]. In Figure 14 instead of t, the quantity $-t+t_{min}$ is again used, where $-t_{min}$ denotes the minimum value of $-t$ for a given Q^2 and $x_{\rm B}$. The different panels in Figure 14 correspond to the different Q^2 and x bins. In the calculations we use the cut-off $\Lambda^2_{\gamma\pi\pi} = 0.46$ GeV^2 in the pion form factor, Eq. (14). This is an optimal value needed for the description of high Q^2 data at JLAB. In Figure 14 the model results which include both the meson-exchange and R/P-contributions are shown by the solid curves. The dash-dotted and the dashed curves correspond to the longitudinal $\epsilon d\sigma_{\rm L}/dt$ and to the transverse $d\sigma_{\rm T}/dt$ components of the cross section, respectively. The dash-dash-dotted curves describe the results without the R/P-contributions.

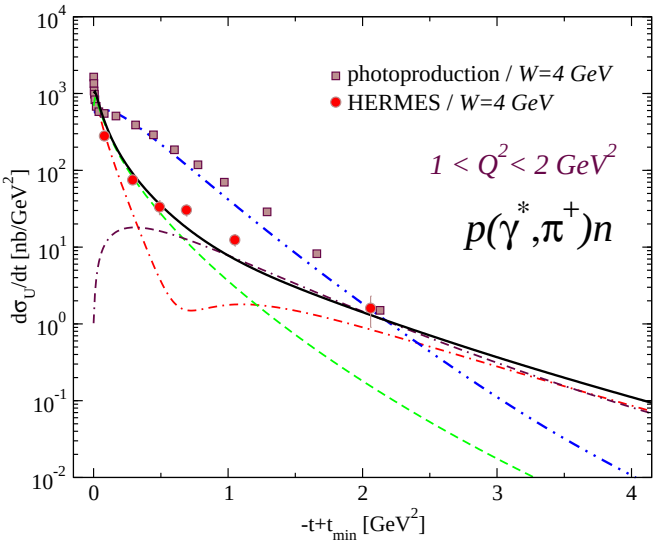

FIG. 15: (Color online) $d\sigma_{\rm U}/dt$ in exclusive reaction $p(\gamma^*,\pi^+)n$ for the average values of $Q^2 = 1.4$ GeV^2 and $x_{\rm B} = 0.08$. The HERMES data, the solid and the dash-dotted curves are the same as in the left panel of Figure 14. The dashed and dash-dash-dotted curves describe the contributions of the π-exchange and resonance/partonic mechanisms to $\epsilon d\sigma_{\rm L}/dt$, respectively. The dot-dot-dashed curve describe the π^+ photoproduction for $E_\gamma = 8$ GeV ($W \simeq 4$ GeV). The photoproduction data are from [54].

Interestingly, the physics of $p(\gamma^*,\pi^+)n$ in the DIS region at HERMES is essentially the same as at JLAB where the value of W is smaller (2 GeV *vs.* 4 GeV). Just contrary to the situation in the JLAB experiment the longitudinal cross section at HERMES determines the total differential cross section at small $-t$. As at JLAB the transverse cross section at HERMES is dominated by the R/P-mechanism. At JLAB the transverse cross section is somewhat larger and at forward angles comparable with the longitudinal cross section. In deeply virtual production of π^+ at HERMES the transverse cross section gets smaller at forward angles and the cross section is dominated by the exchange of Regge trajectories, with π being the dominant trajectory. The π-reggeon exchange contributes mainly to the longitudinal response $\sigma_{\rm L}$ and at low momentum transfer $-t$ the variation of the forward cross section with Q^2 falls down as the electromagnetic form factor of the pion $\sigma_{\rm L} \propto (F_{\gamma\pi\pi}(Q^2))^2$. In the off-forward region, $-t > 1$ GeV^2, because of the exponential

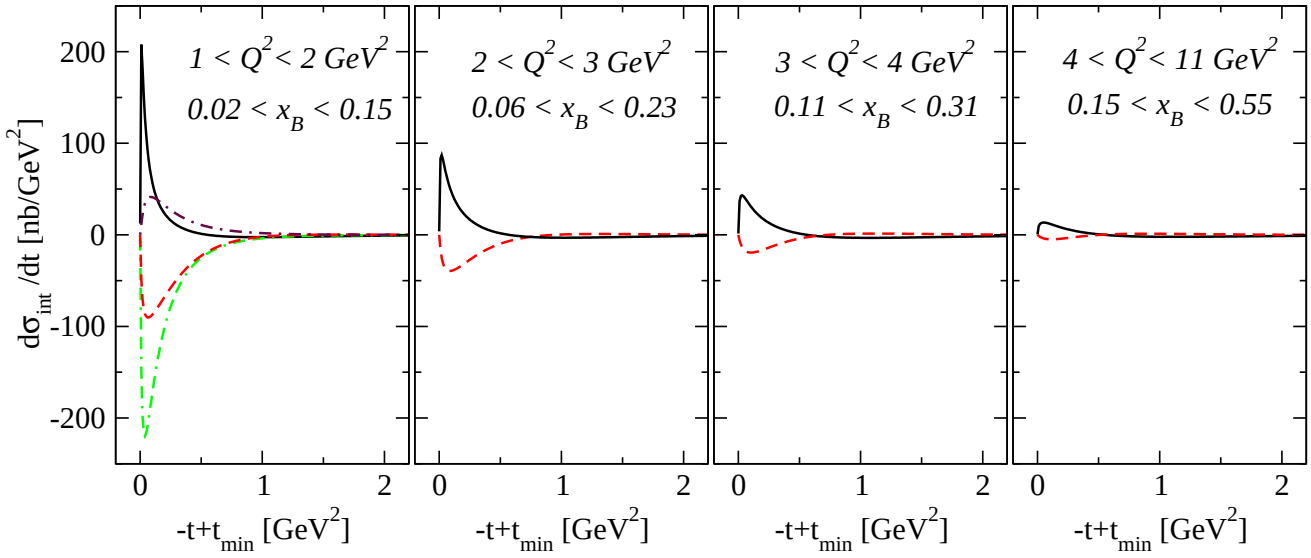

FIG. 16: (Color online) $-t+t_{min}$ dependence of the interference cross sections $d\sigma_{\rm TT}$ (dashed curves) and $d\sigma_{\rm LT}$ (solid curves) at HERMES. The average values of Q^2 and $x_{\rm B}$ used for different $(Q^2, x_{\rm B})$ bins are the same as in Figure 14. In the left panel the dash-dotted and dash-dash-dotted curves describe the contribution of the π-reggeon exchange to $d\sigma_{\rm TT}$ and $d\sigma_{\rm LT}$, respectively.

fall-off of Regge contributions as a function of $-t$, the meson-exchange processes are already negligible. Above $-t > 1$ GeV^2 the model cross section points mainly toward the direct coupling of the virtual photons to partons. Indeed, this is rather natural, since with increasing $-t$ at fixed Q^2 smaller distances can be accessed. This is opposed to t-channel meson-exchange processes which involve peripheral production of π^+.

Contrary to the two-component model of Ref. [27], in the present model there is a sizable longitudinal R/P-component which is effective in the off-forward π^+ production at low values of Bjorken $x_{\rm B}$. For instance, the dip in $\varepsilon d\sigma_{\rm L}/dt$, see the dash-dotted curves in Figure 14, results from the interference between the meson-exchange and the R/P-contributions. In Figure 15 we show the different contributions to $\varepsilon d\sigma_{\rm L}/dt$ for the lowest $x_{\rm B}$ bin. The solid and dash-dotted curves in Figure 15 are the same as in Figure 14 (left panel). The contribution of the π-exchange to $\varepsilon d\sigma_{\rm L}/dt$ is shown by the dashed curve. The latter falls exponentially down as a function of $-t$. The dash-dash-dotted curve describe the R/P-contribution to $\varepsilon d\sigma_{\rm L}/dt$. It vanishes at forward angles and by the destructive interference with the π-reggeon exchange produces a dip in $\varepsilon d\sigma_{\rm L}/dt$. With increasing $-t$ the partonic component of $\varepsilon d\sigma_{\rm L}/dt$ continues to dominate the longitudinal response.

In Figure 15 the dot-dot-dashed curve describes the real photon limit $Q^2 = 0$ of the model cross section for $E_\gamma = 8$ GeV ($W \simeq 4$ GeV). The photoproduction data are from Ref. [54]. This is the same W region as in the HERMES electroproduction data. The model is in agreement with both the photo- and electroproduction data.

In Figure 16 we present the results for the interference cross sections at HERMES energies. $d\sigma_{\rm TT}/dt$ and $d\sigma_{\rm LT}/dt$ are sizable, and follow a behavior observed already at JLAB energies. For instance, if the cross section would be dominated by the π-reggeon exchange then $d\sigma_{\rm TT}/dt$ would be positive (dash-dotted curves in the left panel) and $d\sigma_{\rm LT}/dt$ negative (dash-dash-dotted curves in the left panel). The interference between the π-trajectory and R/P-contributions change the sign of both $d\sigma_{\rm TT}/dt$ and $d\sigma_{\rm LT}/dt$. The solid and dashed curves describe the model results for $d\sigma_{\rm LT}/dt$ and $d\sigma_{\rm TT}/dt$, respectively.

X. Q^2 DEPENDENCE OF THE CROSS SECTIONS

It has been proposed that the Q^2 dependence of L/T separated exclusive $p(\gamma^*, \pi^+)n$ cross sections may provide a test of the factorization theorem [19] in the separation of long-distance and short-distance physics and the extraction of GPD. The leading twist GPD scenario predicts for $\sigma_{\rm L} \sim 1/Q^6$ and $\sigma_{\rm T} \sim 1/Q^8$. An observation of the Q^2 power law scaling is considered as a model independent test of QCD factorization.

The Q^2 behavior of cross sections in exclusive reaction $p(\gamma^*, \pi^+)n$ has been studied at JLAB in Ref. [3]. It was shown that while the scaling laws are reasonably consistent with the Q^2 dependence of the longitudinal $\sigma_{\rm L}$ data, they fail to describe the Q^2 dependence of the transverse $\sigma_{\rm T}$ data. The Q^2 dependence of the $p(\gamma^*, \pi^+)n$ cross section in DIS has been also studied at HERMES [57]. It was found that the Q^2 dependence of the data is in general well described by the calculations from GPD models which include the power corrections, see Ref. [57] and references therein. However, the magnitude of the theoretical cross section is underestimated. The Regge model of Ref. [38] was shown to be compatible with, both, $-t$ and Q^2 dependencies of the HERMES data. In the following

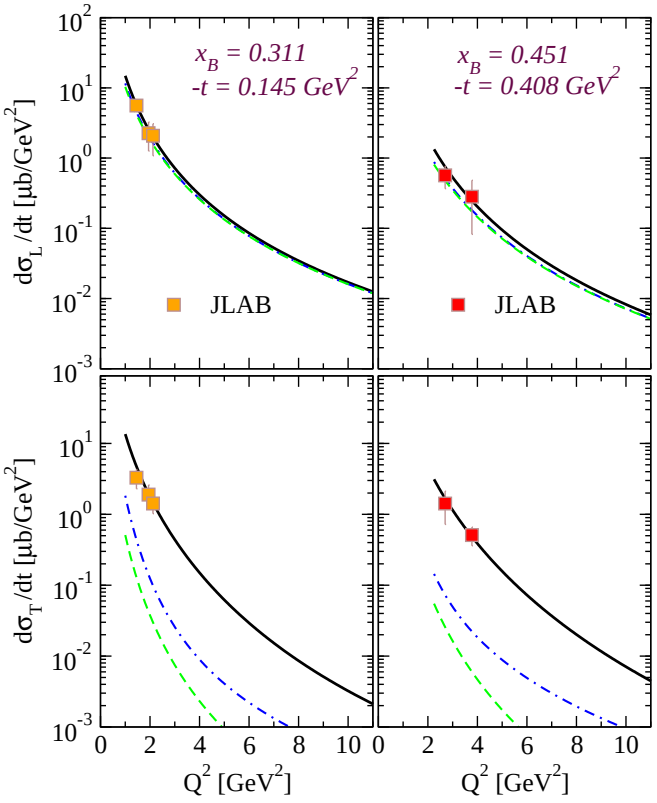

FIG. 17: (Color online) Q^2 dependence of the longitudinal $d\sigma_{\rm L}/dt$ (top panels) and transverse $d\sigma_{\rm T}/dt$ (bottom panels) cross sections in $p(\gamma^*,\pi^+)n$ reaction at fixed values of $-t$ and Bjorken $x_{\rm B}$. The solid curves are the model predictions for the scaling curves. The dashed curves correspond to the contribution of the π-reggeon exchange alone. The dash-dotted curves are the model results without the contributions of resonances. The experimental data are from Ref. [3].

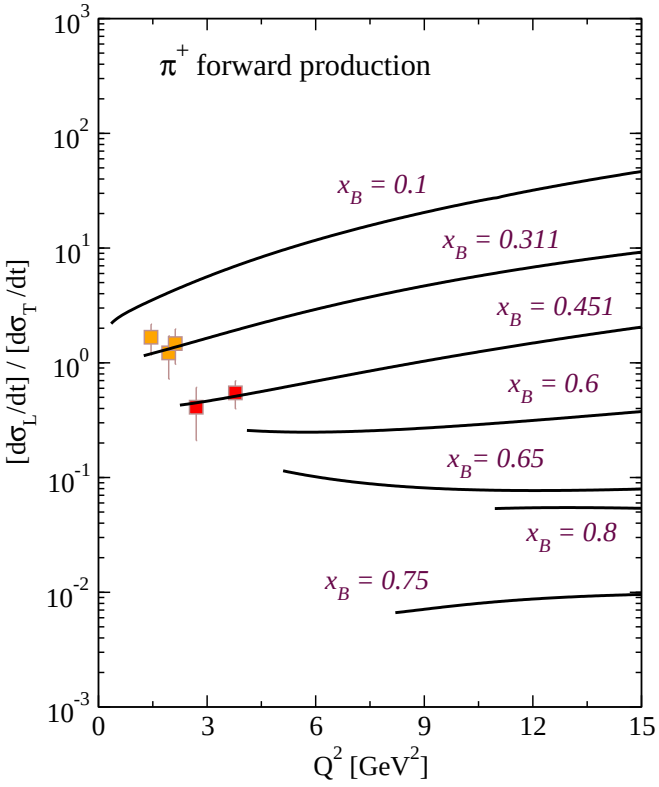

FIG. 18: (Color online) The Q^2 dependence of the ratio of longitudinal $d\sigma_{\rm L}/dt$ to transverse $d\sigma_{\rm T}/dt$ differential cross sections in the forward π^+ production. The different curves correspond to different values of Bjorken scaling variable $x_{\rm B}$.

we check this predicted $\sigma_{\rm L}/\sigma_{\rm T} \sim Q^2$ scaling within our model calculations.

A. JLAB data

In Figure 17 we show our results for the Q^2 dependence of $p(\gamma^*,\pi^+)n$ reaction cross sections $d\sigma_{\rm L}/dt$ and $d\sigma_{\rm T}/dt$ at fixed $-t$ and Bjorken variable x_B. The experimental data are from Ref. [3] and correspond to the forward π^+ production. The solid curves are the model predictions and describe the available data very well. The dashed curves describe the contribution of the π-reggeon exchange to the Q^2 scaling curves only. The dash-dotted curves are the model results without the resonance contributions. The latter effect is again large in the transverse cross section and gives only small correction to the longitudinal cross section $d\sigma_{\rm L}/dt$. The Q^2 dependence of $d\sigma_{\rm L}/dt$ is essentially driven by the pion form factor.

The Q^2 dependence of the ratio of longitudinal $d\sigma_{\rm L}/dt$ to transverse $d\sigma_{\rm T}/dt$ differential cross sections for the forward π^+ production is shown in Figures 18. The different curves correspond to different values of $x_{\rm B}$. All the curves start at the value of $W \simeq 1.9$ GeV. For small and intermediate values of $x_{\rm B}$ the model results show an increase of the ratio $d\sigma_{\rm L}/d\sigma_{\rm T}$ as a function of Q^2. Only at small values of Bjorken $x_{\rm B}$ the ratio $d\sigma_{\rm L}/d\sigma_{\rm T}$ is qualitatively in agreement with the predicted $\sim Q^2$ behavior. In the valence quark region above $x_{\rm B} \simeq 0.6$ the cross section ratio scales and is actually independent of the value of Q^2. In this region the transverse component $\sigma_{\rm T}$ dominates the π^+ electroproduction cross section. In the experimental determination of the pion transition form factor from forward $\sigma_{\rm L}$ data one can, therefore, better isolate the longitudinal response by minimizing the Bjorken $x_{\rm B}$.

B. HERMES data

In Section IX we concluded that the physics content of the HERMES deep exclusive $p(\gamma^*,\pi^+)n$ data is essentially the same as at JLAB. Figure 19 shows the Q^2 dependence of the measured cross sections in DIS for different $x_{\rm B}$ bins [7, 57]. These are the same data sets from HERMES (see previous section) integrated over $-t$. The Q^2 dependence of the experimental data is well described by the calculations (solid curves) from the present model. The dashed and dash-dotted curve describe the longitudi-

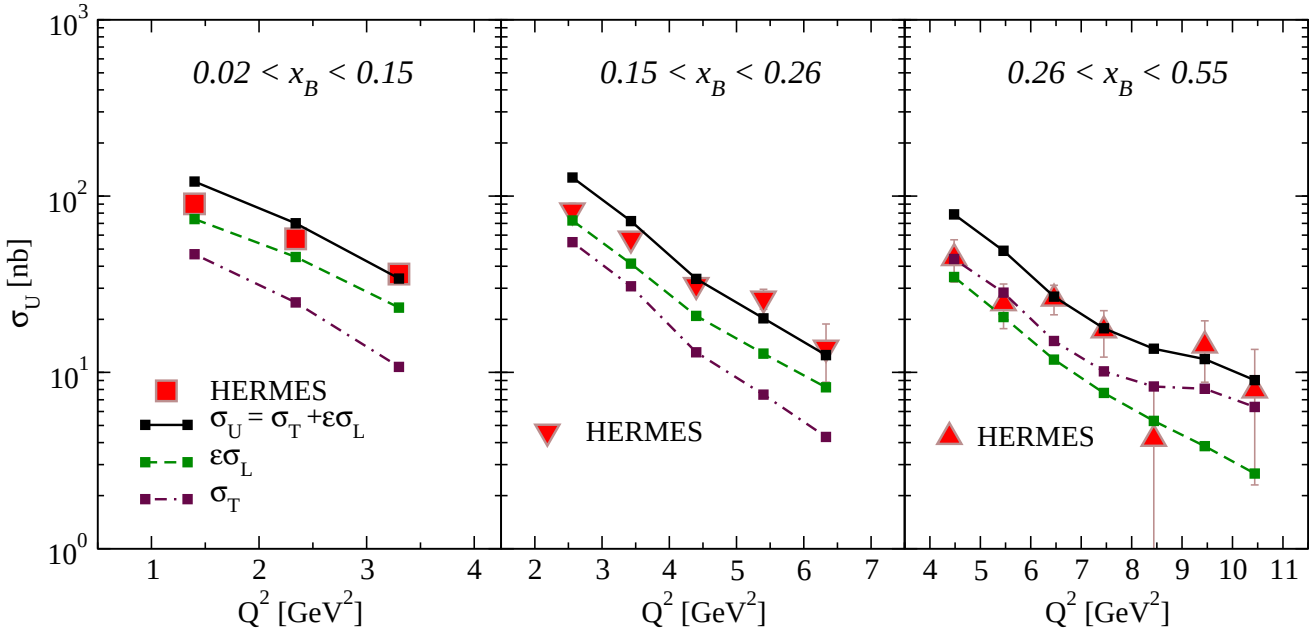

FIG. 19: (Color online) Q^2 dependence of the integrated cross sections $\sigma_{\rm U} = \sigma_{\rm T} + \epsilon\sigma_{\rm L}$ in exclusive reaction $p(\gamma^*, \pi^+)n$ at HERMES. The different panels correspond to different x_B bins. The solid curves are the model results. The dashed and dash-dotted curves correspond to the longitudinal $\epsilon\sigma_{\rm L}$ and transverse $\sigma_{\rm T}$ components of the cross section, respectively. The experimental data are from Ref. [7]

nal $\varepsilon\sigma_{\rm L}$ and the transverse $\sigma_{\rm T}$ components, respectively.

In the region of small Bjorken $x_{\rm B}$, see left panel in Figure 19, the integrated longitudinal component dominates over the transverse cross section. With increasing $x_{\rm B}$ the strength of the transverse component is increasing and for values of x_B in the third bin the transverse cross section $\sigma_{\rm T}$ becomes the dominant part of the exclusive cross section. An increase of the relative contribution of $\sigma_{\rm T}$ as a function of $x_{\rm B}$ can be clearly seen in the right panel of Figure 19 where $0.26 < x_{\rm B} < 0.55$. There the first Q^2 bin corresponds to the average value of $x_{\rm B} = 0.29$ and the last Q^2 bin to the average value of $x_{\rm B} = 0.44$ [57].

XI. BEAM SPIN ASYMMETRY

In this work we have restricted ourselves to exclusive $(e, e'\pi^{\pm})$ reactions with an unpolarized target. With a polarized beam $(\vec{e}, e'\pi^{\pm})$ and with an unpolarized target there is an additional component $\sigma_{\rm LT'}$, Eq. (3), which is proportional to the imaginary part of an interference between the L/T photons and therefore sensitive to the relative phases of amplitudes.

In general, a nonzero $\sigma_{\rm LT'}$ or the corresponding beam SSA $A_{\rm LU}(\phi)$, Eq. (7), demands interference between single helicity flip and nonflip or double helicity flip amplitudes. In Regge models the asymmetry may result from Regge cut corrections to single reggeon exchange [58]. This way the amplitudes in the product acquire different phases and therefore relative imaginary parts. A nonzero beam SSA can be also generated by the interference pattern of amplitudes where particles with opposite parities are exchanged.

In the following we discuss briefly the generic features of the beam SSA in the present model. The comparative analysis of the SSA at JLAB and HERMES will be presented in the forthcoming publication.

In the left panel of Figure (20) we plot the CLAS data [6] for the azimuthal moment $A_{\rm LU}^{\sin(\phi)}$ associated with the beam SSA, Eq. (8), in the reaction $p(\vec{e}, e'\pi^+)n$. These data have been collected in hard scattering kinematics $E_e = 5.77$ GeV, $W > 2$ GeV and $Q^2 > 1.5$ GeV^2. The experiment shows a sizable and positive beam SSA. In the left and right panels of Figure (20) we present the results for the azimuthal moments $A_{\rm LU}^{\sin(\phi)}$ in the reactions $p(\vec{e}, e'\pi^+)n$ and $n(\vec{e}, e'\pi^-)p$, respectively. The (Q^2, W) binning of the experimental data point is not available. In the following the calculations are done for the lowest (Q^2, W) bin corresponding to the values of $Q^2 = 1.5$ GeV^2 and $W^2 = 4$ GeV^2.

At first, we consider $A_{\rm LU}^{\sin(\phi)}$ generated by the exchange of Regge trajectories. In Figure (20) the dashed curves describe the model results without the R/P-effects and neglecting the exchange of the axial-vector $a_1(1260)$ Regge trajectory. This model results in a zero $A_{\rm LU}^{\sin(\phi)}$ and therefore a zero beam SSA. The addition of the unnatural parity $a_1(1260)$-exchange generates by the interference with the natural parity $\rho(770)$ exchange a sizable $A_{\rm LU}^{\sin(\phi)}$ in both channels. This result corresponds to the dash-dotted curves in Figure (20). In the rest of observables discussed above the effect of the axial-

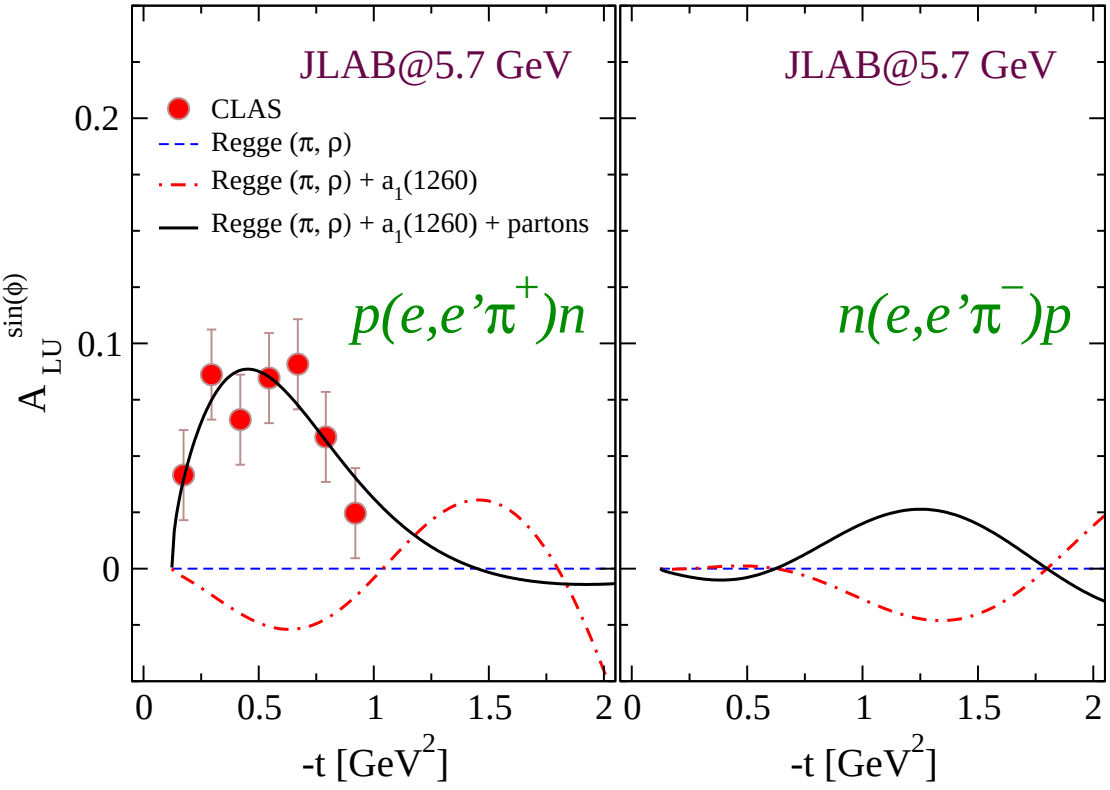

FIG. 20: (Color online) Left panel: The beam spin azimuthal moment $A_{\rm LU}^{\sin(\phi)}$ in exclusive reaction $p(\gamma^*,\pi^+)n$ as a function of $-t$. The CLAS/JLAB data [6] were collected for hard scattering kinematics with values of $E_e = 5.77$ GeV, $Q^2 > 1.5$ GeV^2 and $W^2 > 4$ GeV^2. The dashed curves describe the results (the asymmetry is zero) without the resonance contributions and neglecting the exchange of unnatural parity $a_1(1260)$ Regge trajectory. The dash-dotted curves correspond to the addition of the axial-vector $a_1(1260)$-reggeon exchange. The solid curves are the model results and account for the resonance/partonic effects. Right panel: The beam spin azimuthal moment $A_{\rm LU}^{\sin(\phi)}$ in exclusive reaction $n(\gamma^*,\pi^-)p$. The notations for the curves are the same as in the left panel.

vector $a_1(1260)$ is small. However, as one can see, the contribution of $a_1(1260)$ is important in the polarization observables. For instance, a strong interference pattern of the $a_1(1260)$-reggeon exchange makes the polarization observables, like the beam SSA, very sensitive to the different scenarios [45] describing the structure and behavior of $a_1(1260)$ in high-Q^2 processes.

In the last step we account for the R/P-contribution. The latter strongly influence the asymmetry parameter $A_{\rm LU}^{\sin(\phi)}$. The model results (solid curves) are in agreement with the positive $A_{\rm LU}^{\sin(\phi)}$ in the π^+ channel and predict much smaller $A_{\rm LU}^{\sin(\phi)}$ in the π^- channel. A sizable and positive $A_{\rm LU}^{\sin(\phi)}$ has been also observed at HERMES in π^+ SIDIS close to the exclusive limit $z \to 1$ [59].

XII. A BENCHMARK FOR JLAB AT 12 GEV: $p(\gamma^*,\pi^+)n$ AT CORNELL

A forthcoming upgrade of the JLAB to 12 GeV will allow to measure $p(e,e'\pi^+)n$ and $n(e,e'\pi^-)p$ reactions for values of $Q^2 = 1.6 \div 6.0$ GeV^2 and W near 3 GeV [56]. This is just an intermediate region between the present JLAB and the deep exclusive HERMES data. In this (Q^2, W) region there are old Cornell data [10] around $W \simeq 3.1$ GeV and values of $Q^2 \simeq 1.2$ and 1.7 GeV^2. These data may serve as a benchmark for the JLAB at 12 GeV predictions.

Figure 21 shows the Cornell data [10] and the calculated differential cross sections for the electroproduction of π^+ meson as a function of $-t$. As an example, we selected data with the virtual-photoproduction planes of the emitted pions in average parallel $-45^\circ < \phi < 45^\circ$ to the electron scattering plane. The solid curves in Figure 21 describe the model results and the dashed curves correspond to the results without the resonance contributions. The cross sections have been integrated over the corresponding range of azimuthal out-of-plane angles. Figure 22 shows the calculated ratio of π^- and π^+ differential cross sections (solid curve) as a function of $-t$. The data are from [10]. As in Figure 21 the cross sections have been integrated over the range of azimuthal out-of-plane acceptance $-45^\circ < \phi < 45^\circ$.

The difference between the solid and dashed curves in Figure 21 comes from the contribution of reso-

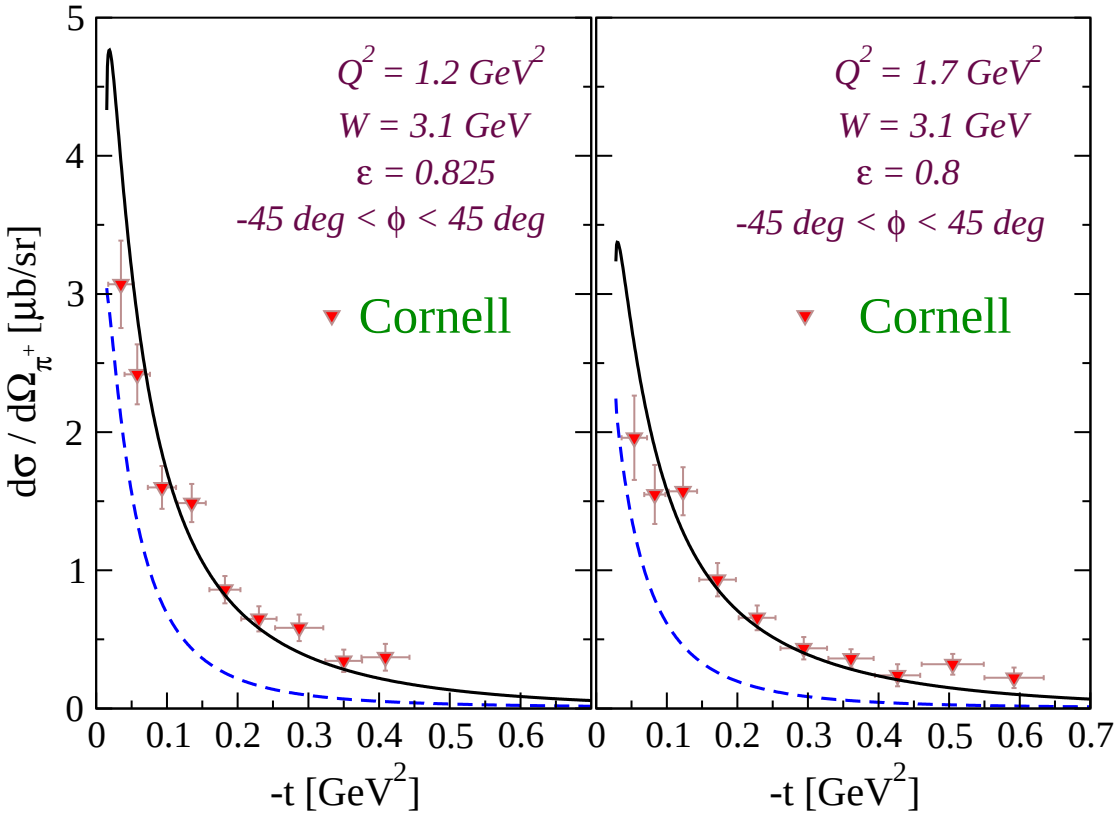

FIG. 21: (Color online) The differential cross sections for the electroproduction of π^+ meson at Cornell. The solid curves describe the model results and the dashed curves correspond to the results without the resonance/partonic contributions. The data are from [10]. The values of (W, Q^2, ε) are the average ones. The theoretical cross sections have been integrated over the range of azimuthal out-of-plane acceptance $-45^\circ < \phi < 45^\circ$.

nances. The latter effect is expected to be important at JLAB@12, see Section XIII for the results.

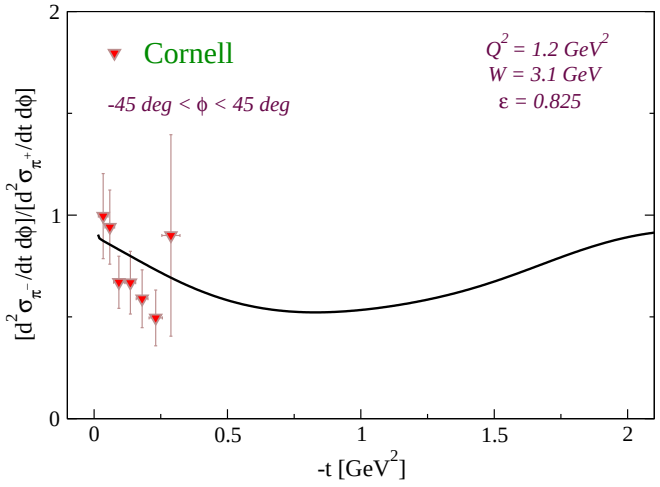

FIG. 22: (Color online) The π^-/π^+ ratio of differential cross sections for the electroproduction of π^- and π^+ mesons at Cornell. The data are from [10]. The theoretical cross section has been integrated over the range of azimuthal out-of-plane acceptance $-45^\circ < \phi < 45^\circ$.

XIII. JLAB AT 12 GEV

Finally, in this section we provide the predictions for the L/T separated $\pi^\pm$ differential cross sections at forward angles in the (Q^2, W) kinematics proposed for the forthcoming $F\pi$-12 experiment [56] at JLAB. The primary goal of the measurements is an extraction of the pion form factor from the longitudinal data at high values of Q^2.

In Figures 23 and 24 we plot the $-t + t_{min}$ dependence of the L/T partial differential cross sections $d\sigma_{\rm T}/dt$ (solid), $d\sigma_{\rm L}/dt$ (dashed), $d\sigma_{\rm LT}/dt$ (dash-dotted) and $d\sigma_{\rm TT}/dt$ (dash-dash-dotted) in the reactions $p(\gamma^*, \pi^+)n$ and $n(\gamma^*, \pi^-)p$, respectively. In these calculations we used the value of $\Lambda^2_{\gamma\pi\pi} = 0.46$ GeV^2.

As one can see, at JLAB@12 in exclusive reaction $p(\gamma^+, \pi^+)n$ the transverse cross section $d\sigma_{\rm T}/dt$ gets smaller compared to JLAB@5, see solid curves in Figures 23. But $d\sigma_{\rm T}/dt$ still gives important contributions at forward angles. The ratios $R = d\sigma_{\rm T}/d\sigma_{\rm L}$ of the transverse and longitudinal cross sections at forward π^+ angles $t = t_{min}$ for W reached at JLAB@5 and JLAB@12 are compared in Table II. For the comparison the values of $Q^2 = 1.6$ and 2.45 GeV^2 are used. With increasing value of W at fixed Q^2 the ratio gets smaller and makes an

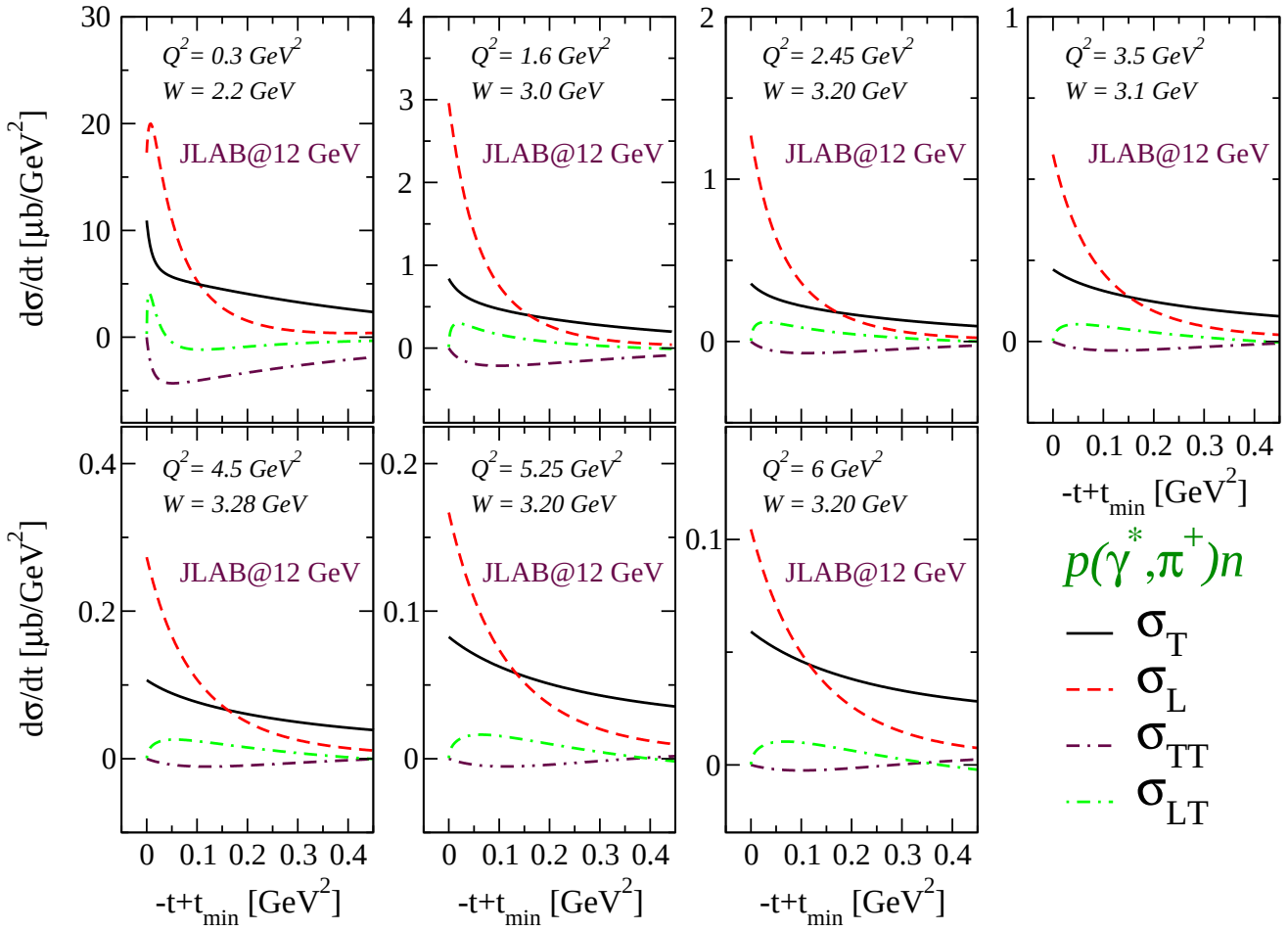

FIG. 23: (Color online) $-t+t_{min}$ dependence of L/T separated differential cross sections $d\sigma_{\rm T}/dt$ (solid), $d\sigma_{\rm L}/dt$ (dashed), $d\sigma_{\rm LT}/dt$ (dash-dotted) and $d\sigma_{\rm TT}/dt$ (dash-dash-dotted) in exclusive reaction $p(\gamma^*,\pi^+)n$ in the (Q^2,W) kinematics at JLAB@12.

accurate determination of the longitudinal cross section needed for the extraction of the pion from factor feasible.

In the π^- channel the contribution of the tranverse and interference cross sections is predicted to be much smaller. As one can see in Figure 24 the π^- electroproduction cross section is largely longitudinal (dashed curves). If true this may provide a complimentary and probably more reliable access to the pion form factor from exclusive π^- electroproduction off the deuteron target.

JLAB	Q^2 [GeV^2]	W [GeV]	$R=d\sigma_{\rm T}/d\sigma_{\rm L}$
5 GeV	1.60	2.2	0.43
	2.45	2.2	0.68
12 GeV	1.60	3.0	0.28
	2.45	3.0	0.32

TABLE II: The ratio $R=d\sigma_{\rm T}/d\sigma_{\rm L}$ of the transverse and longitudinal cross sections at forward angles $t=t_{min}$ in a kinematics of JLAB@5 with $W=2.2$ GeV and JLAB@12 with $W=3$ GeV and values of $Q^2=1.6$ and 2.45 GeV^2.

XIV. SUMMARY

In summary, a description of exclusive charged pion electroproduction $(e,e'\pi^\pm)$ off nucleons at high energies is proposed. Following a two-component hadron-parton picture of Refs. [25, 27] the model combines a Regge pole approach with residual effects of nucleon resonances. The contribution of nucleon resonances has been assumed to be dual to direct partonic interaction and therefore describes the hard part of the model cross sections. The resonance/partonic effects are taken into account using a Bloom-Gilman connection between the exclusive hadronic form factors and inclusive deep inelastic structure functions. In the soft hadronic sector the exchanges of $\pi(140)$, vector $\rho(770)$ and axial-vector $a_1(1260)$ and $b_1(1235)$ Regge trajectories have been considered.

We have shown that with only a few physical assumptions a quantitative description of exclusive π^+ and π^- electroproduction data can be achieved in a large range of (Q^2,W) from JLAB to DIS region at HERMES. In particular, the L/T partial longitudinal, transverse and interference cross sections measured at JLAB and DESY

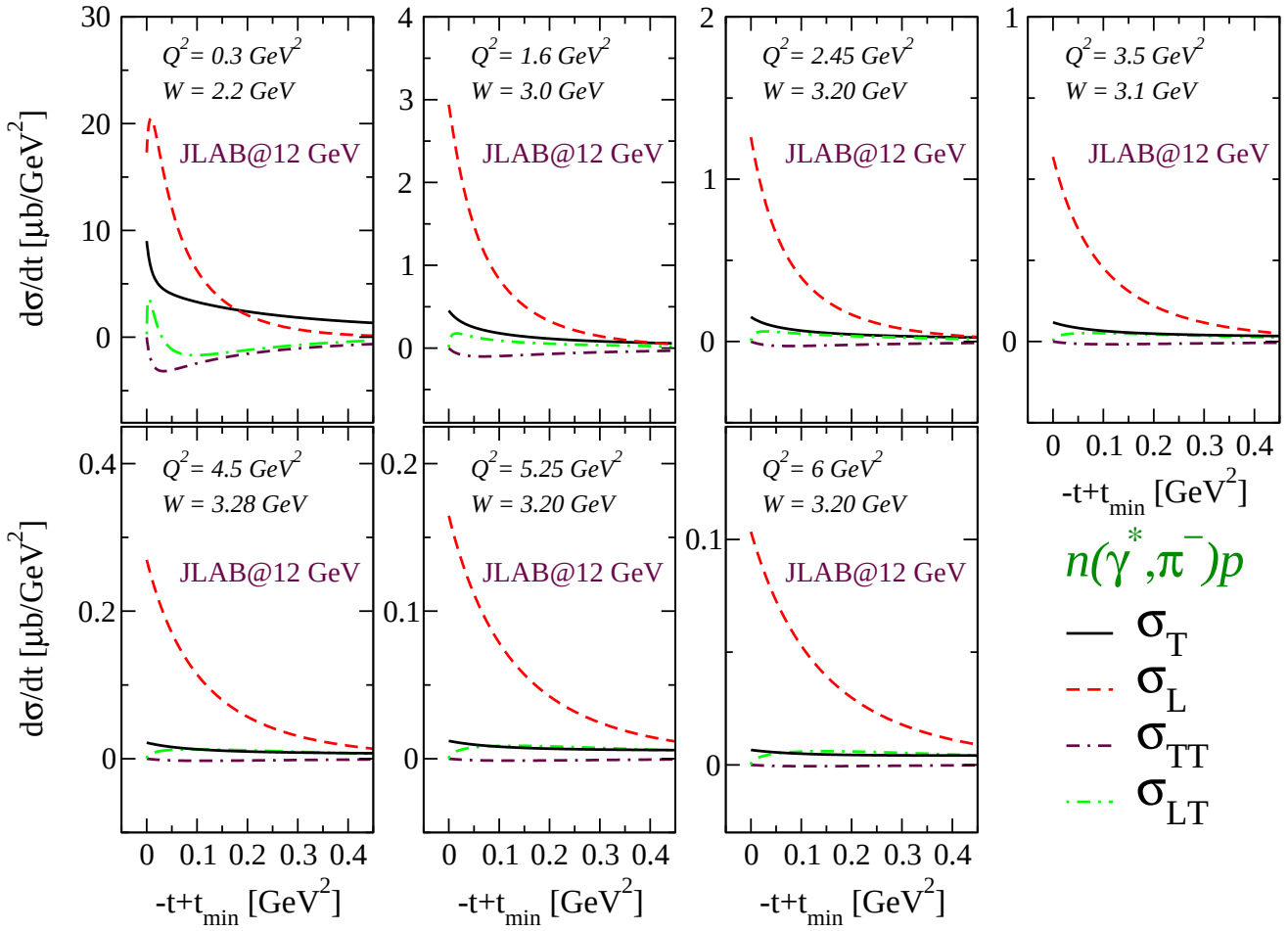

FIG. 24: (Color online) $-t + t_{min}$ dependence of L/T separated differential cross sections $d\sigma_{\rm T}/dt$ (solid), $d\sigma_{\rm L}/dt$ (dashed), $d\sigma_{\rm LT}/dt$ (dash-dotted) and $d\sigma_{\rm TT}/dt$ (dash-dash-dotted) in exclusive reaction $n(\gamma^*,\pi^-)p$ in the (Q^2, W) kinematics at JLAB@12.

are reproduced. Our principal result is that a longstanding problem concerning the description of the transverse and interference cross sections can be solved by the resonance/partonic effects in line of the DIS mechanism proposed in [25, 27]. However, the present model goes beyond the two-component approach of [25, 27] and allows to treat the resonance/partonic contributions on the amplitude level. The latter show up as a large transverse background contribution to the π quasi-elastic knockout mechanism. As in [25, 27], we find that at high values of Q^2 the resonances dominate in $\sigma_{\rm T}$.

The contribution of resonances in the forward longitudinal response $\sigma_{\rm L}$ is rather small and makes an experimental isolation of the pion-pole amplitude and the pion transition form factor in the region of Bjorken $x_{\rm B} < 0.5$ feasible. The interference pattern of the π-exchange and resonance contributions is sufficient to explain the sign and magnitude of the interference $\sigma_{\rm TT}$ and $\sigma_{\rm LT}$ cross sections measured at JLAB and DESY. The same resonance/partonic mechanism is responsible for the positive azimuthal beam SSA observed in $p(\vec{e}, e'\pi^+)n$. On the contrary, the beam SSA in deep exclusive π^- production off the neutrons is predicted to be much smaller in magnitude and very sensitive to the different scenarios concerning the structure of the $a_1(1260)$ meson.

The Q^2 behavior of the model exclusive $p(\gamma^*,\pi^+)n$ reaction cross sections is in agreement with JLAB and deeply virtual HERMES data.

We have furthermore calculated the ratio of π^-/π^+ cross sections which is of present interest in the dedicated experiments at JLAB. Model predictions for JLAB at 12 GeV are also provided. On the experimental side, the present results may be used as a guideline in the experimental analysis of background contributions to the π quasi-elastic knockout mechanism. The latter is important for the extraction of the pion transition form factor to minimize systematic uncertainties.

Acknowledgments

This work was supported by DFG through the SFB/TR16.

Appendix A: The partial virtual-photon nucleon cross sections

The longitudinal/transverse (L/T) separated photon-nucleon cross sections take the forms

$$\frac{1}{\mathcal{N}}\frac{d\sigma_{\rm L}}{dt} = \overline{(J^\mu \epsilon^0_\mu J^{\nu\dagger}\epsilon^{\dagger 0}_\nu)}, \tag{A1}$$

$$\frac{1}{\mathcal{N}}\frac{d\sigma_{\rm T}}{dt} = \frac{1}{2}\sum_{\lambda=\pm 1}\overline{(J^\mu \epsilon^\lambda_\mu J^{\nu\dagger}\epsilon^{\dagger\lambda}_\nu)}, \tag{A2}$$

$$\frac{1}{\mathcal{N}}\frac{d\sigma_{\rm TT}}{dt} = -\frac{1}{2}\sum_{\lambda=\pm 1}\overline{(J^\mu \epsilon^\lambda_\mu J^{\nu\dagger}\epsilon^{\dagger -\lambda}_\nu)}, \tag{A3}$$

$$\frac{1}{\mathcal{N}}\frac{d\sigma_{\rm LT}}{dt} = -\frac{1}{2\sqrt{2}}\sum_{\lambda=\pm 1}\lambda[\overline{(J^\mu \epsilon^0_\mu J^{\nu\dagger}\epsilon^{\dagger\lambda}_\nu)} + \overline{(J^\mu \epsilon^\lambda_\mu J^{\nu\dagger}\epsilon^{\dagger 0}_\nu)}], \tag{A4}$$

$$\frac{1}{\mathcal{N}}\frac{d\sigma_{\rm LT'}}{dt} = -\frac{1}{2\sqrt{2}}\sum_{\lambda=\pm 1}\lambda[\overline{(J^\mu \epsilon^0_\mu J^{\nu\dagger}\epsilon^{\dagger\lambda}_\nu)} - \overline{(J^\mu \epsilon^\lambda_\mu J^{\nu\dagger}\epsilon^{\dagger 0}_\nu)}], \tag{A5}$$

where $\overline{(...)}$ stands for the sum and average over the initial and final nucleon spins. The normalization factor reads

$$\mathcal{N} = \frac{\alpha_e}{4\pi}\frac{2\pi M_N^2}{(W^2 - M_N^2)Wq^*}, \tag{A6}$$

where q^* is a three momentum of the incoming virtual photon in the $\gamma^* N$ center of mass frame. ϵ^λ_μ are the basis vectors of circular polarization for the virtual photon with helicities $\lambda = \pm 1, 0$ quantized along the three momentum $\vec{q}$, *i.e.*,

$$\epsilon^\pm_\mu = \mp\frac{1}{\sqrt{2}}(0, 1, \pm i, 0), \tag{A7}$$

$$\epsilon^0_\mu = \frac{1}{\sqrt{Q^2}}(\sqrt{\nu^2 + Q^2}, 0, 0, \nu), \tag{A8}$$

and J^μ is the nuclear transition axial-vector current describing the pion production in the momentum space.

Appendix B: On the gauged electric amplitude

The Lorentz tensor-vector decomposition of the nucleon-pole term in Eq. (9) is given by

$$\bar{u}_{s'}(p')\gamma_5\frac{(p+q)_\sigma\gamma^\sigma\gamma^\mu + M_p\gamma^\mu}{s - M_p^2 + i0^+}u_s(p) = \bar{u}_{s'}(p')\gamma_5\left[\frac{i\sigma^{\mu\sigma}q_\sigma}{s - M_p^2 + i0^+} + \frac{(p + p' + k')^\mu}{s - M_p^2 + i0^+}\right]u_s(p), \tag{B1}$$

where $\sigma^{\mu\sigma} = \frac{i}{2}[\gamma^\mu, \gamma^\sigma]$. The axial-tensor term in the *r.h.s.* of Eq. (B1) is gauge invariant by itself. It turns out that only the orbital part proportional to $p+p'+k'$ is needed to conserve the charge in the sum with the π-pole amplitude, the first term in Eq. (9). In photoproduction the orbital part has no physical significance because it appears in the physical scattering amplitude multiplied by the polarization vector ϵ^λ_μ. Since, $q^\mu\epsilon^\pm_\mu = p^\mu\epsilon^\pm_\mu = 0$ the product $(p + p' + k')\epsilon^\pm_\mu = (2p + q)\epsilon^\pm_\mu = 0$. The nucleon-pole term generates a large axial-tensor background to the meson-pole amplitude which has important consequences in photoproduction. For instance, since the interference of π with $\rho(770)$ is trivially zero it is $\sigma^{\mu\sigma}\gamma_5$ in the nucleon-pole term which, by interference with ρ, is responsible for the π^-/π^+ asymmetry. It is also this term which explains the forward peak in the forward $\pi^\pm$ production and the rapid variation of the polarized photon asymmetry in the same region.

[1] T. Horn *et al.*, Phys. Rev. Lett. **97**, 192001 (2006).
[2] V. Tadevosyan *et al.*, Phys. Rev. C **75**, 055205 (2007).
[3] T. Horn *et al.*, Phys. Rev. C **78**, 058201 (2008).
[4] H. P. Blok *et al.*, Phys. Rev. C **78**, 045202 (2008).
[5] G. M. Huber *et al.*, Phys. Rev. C **78**, 045203 (2008).
[6] H. Avakian and L. Elouadrhiri [CLAS Collaboration], Phys. Part. Nucl. **35**, S114 (2004).
[7] A. Airapetian *et al.*, Phys. Lett. B **659**, 486 (2008).
[8] C.N. Brown *et al.*, Phys. Rev. D **8**, 92 (1973).
[9] C.J. Bebek *et al.*, Phys. Rev. D **9**, 1229 (1974).
[10] C.J. Bebek *et al.*, Phys. Rev. D **13**, 25 (1976).
[11] C.J. Bebek *et al.*, Phys. Rev. D **17**, 1693 (1978).
[12] H. Ackermann *et al.*, Nucl. Phys. B **137**, 294 (1978).
[13] P. Brauel *et al.*, Phys. Lett. B **65**, 181 (1976).
[14] P. Brauel *et al.*, Phys. Lett. B **65**, 184 (1976).
[15] P. Brauel *et al.*, Phys. Lett. B **69**, 253 (1977).
[16] P. Brauel *et al.*, Z. Phys. C **3**, 101 (1979).
[17] V. G. Neudatchin *et al.*, Nucl. Phys. A **739**, 124 (2004).
[18] J. D. Sullivan, Phys. Lett. B **33**, 179 (1970).
[19] J. C. Collins, L. Frankfurt and M. Strikman, Phys. Rev.

D **56**, 2982 (1997).
[20] O. Nachtmann, Nucl. Phys. B **115**, 61 (1976).
[21] P. D. B. Collins and T. Wilkie, Z. Phys. C **7**, 357 (1981).
[22] A. Faessler *et al.*, Phys. Rev. C **76**, 025213 (2007).
[23] B. Clasie *et al.*, Phys. Rev. Lett. **99**, 242502 (2007).
[24] M. M. Kaskulov, K. Gallmeister and U. Mosel, Phys. Rev. C **79**, 015207 (2009).
[25] M. M. Kaskulov, K. Gallmeister and U. Mosel, Phys. Rev. D **78**, 114022 (2008).
[26] J. D. Bjorken and J. Kogut, Phys. Rev. D **8**, 1341 (1973).
[27] M. M. Kaskulov and U. Mosel, Phys. Rev. C **80**, 028202 (2009) [arXiv:0904.4442 [hep-ph]].
[28] S. V. Goloskokov and P. Kroll, Eur. Phys. J. C **65**, 137 (2010).
[29] M. Guidal, J. M. Laget and M. Vanderhaeghen, Nucl. Phys. A **627**, 645 (1997).
[30] E. D. Bloom and F. Gilman, Phys. Rev. D **4**, 2901 (1971).
[31] E. D. Bloom and F. J. Gilman, Phys. Rev. Lett. **25**, 1140 (1970).
[32] A. Bacchetta, U. D'Alesio, M. Diehl and C. A. Miller, Phys. Rev. D **70**, 117504 (2004).
[33] L. N. Hand, Phys. Rev. **129**, 1834 (1963).
[34] H. Naus and J. H. Koch, Phys. Rev. C **39**, 1907 (1989).
[35] J. H. Koch, V. Pascalutsa and S. Scherer, Phys. Rev. C **65**, 045202 (2002).
[36] F. Gross and D. O. Riska, Phys. Rev. C **36**, 1928 (1987).
[37] L. M. Jones, Rev. Mod. Phys. **52**, 545 (1980).
[38] J. M. Laget, Phys. Rev. D **70**, 054023 (2004).
[39] L. Mankiewicz, G. Piller and A. Radyushkin, Eur. Phys. J. C **10**, 307 (1999).
[40] F.Gutbrod and G.Kramer, Nucl. Phys. B **49**, 461 (1972).
[41] G. Domokos, S. Kovesi-Domokos and E. Schonberg, Phys. Rev. D **3**, 1184 (1971).
[42] M. Elitzur, Phys. Rev. D **3**, 2166 (1971).
[43] L. Y. Glozman, Phys. Rev. Lett. **99**, 191602 (2007).
[44] R. Worden, Nucl. Phys. B **37**, 253 (1972).
[45] C. Bechler and D. Mueller, arXiv:0906.2571 [hep-ph].
[46] W. M. Yao *et al.*, Journal of Physics, **G 33**, 1 (2006).
[47] M. J. Sweig and W. W. Wada, Phys. Rev. Lett. **21**, 414 (1968).
[48] M. Birkel and H. Fritzsch, Phys. Rev. D **53**, 6195 (1996).
[49] M. M. Kaskulov and P. Grabmayr, Phys. Rev. C **67**, 042201 (2003); M. M. Kaskulov and P. Grabmayr, Phys. Rev. C **69**, 028201 (2004).
[50] G. M. Huber, private communication.
[51] F. E. Close and N. Isgur, Phys. Lett. B **509**, 81 (2001).
[52] X. Qian *et al.*, arXiv:0908.1616 [nucl-ex].
[53] M. Vanderhaeghen, M. Guidal and J. M. Laget, Phys. Rev. C **57**, 1454 (1998).
[54] A. Boyarski *et al.*, Phys. Rev. Lett. **20**, 300 (1968).
[55] D. J. Quinn *et al.*, Phys. Rev. D **20**, 1553 (1979).
[56] G. M. Huber *et al.*, "Measurement of the charges pion form factor to high Q^2, JLAB PAC 30 proposal, (2006).
[57] A. Airapetian, private communication.
[58] S. Ahmad, G. R. Goldstein and S. Liuti, Phys. Rev. D **79**, 054014 (2009).
[59] A. Airapetian *et al.*, Phys. Lett. B **648**, 164 (2007).